



PCCP

**Reactive Force Fields for Aqueous and Interfacial  
Magnesium Carbonate Formation**

Journal:	<i>Physical Chemistry Chemical Physics</i>
Manuscript ID	CP-ART-06-2021-002627.R1
Article Type:	Paper
Date Submitted by the Author:	28-Aug-2021
Complete List of Authors:	Zare, Siavash; University of California Irvine, School of Civil and Environmental Engineering Abdolhosseini Qomi, Mohammad Javad; University of California Irvine Henry Samueli School of Engineering,

SCHOLARONE™  
Manuscripts

# 1 Reactive Force Fields for Aqueous and Interfacial Magnesium Carbonate Formation

2 Siavash Zare<sup>1</sup>, Mohammad Javad Abdolhosseini Qomi<sup>1,\*</sup>

3 <sup>1</sup>Department of Civil and Environmental Engineering, University of California, Irvine, CA, United State.

4  
5 **Abstract:** We develop Mg/C/O/H ReaxFF parameter sets for two environments: an aqueous force  
6 field for magnesium ions in solution and an interfacial force field for minerals and mineral-water  
7 interfaces. Since magnesium is highly ionic, we choose to fix the magnesium charge and model its  
8 interaction with C/O/H through Coulomb, Lennard Jones, and Buckingham potentials. We  
9 parameterize the forcefields against several crystal structures, including brucite, magnesite,  
10 magnesia, magnesium hydride, and magnesium carbide, as well as Mg<sup>2+</sup> water binding energies  
11 for the aqueous forcefield. Then, we test the forcefield for other magnesium-containing crystals,  
12 solvent separated and contact ion-pairs and single-molecule/multilayer water adsorption energies  
13 on mineral surfaces. We also apply the forcefield to the forsterite-water and brucite-water interface  
14 that contains a bicarbonate ion. We observe that a long-range proton transfer mechanism  
15 deprotonates the bicarbonate ion to carbonate at the interface. Free energy calculations show that  
16 carbonate can attach to the magnesium surface with an energy barrier of about 0.22 eV, consistent  
17 with the free energy required for aqueous Mg-CO<sub>3</sub> ion pairing. Also, the diffusion constant of the  
18 hydroxide ions in the water layers formed on the forsterite surface are shown to be anisotropic and  
19 heterogeneous. These findings can explain the experimentally observed fast nucleation and growth  
20 of magnesite at low temperature at the mineral-water-CO<sub>2</sub> interface in water-poor conditions.

## 21 1- Introduction

22 Magnesium is an abundant alkaline-earth metal that plays a pivotal role in biological processes(1),  
23 automotive industry(2), battery technology(3), and mineral carbonation(4). In particular, mineral  
24 carbonation in geological systems has gained considerable attention during the past two decades  
25 amid the record-high CO<sub>2</sub> concentration in the atmosphere. Carbonation is the reaction between  
26 CO<sub>2</sub> and Me<sup>2+</sup>-containing minerals through natural weathering or geological sequestration that  
27 produces stable carbonate minerals. When dissolved in water, divalent metal cations like Mg<sup>2+</sup> and  
28 Ca<sup>2+</sup> bind to water molecules or negatively charged anions like carbonate anions. The pairing  
29 between magnesium/calcium and carbonate is a precursor for the precipitation of calcite (CaCO<sub>3</sub>),  
30 dolomite (CaMg(CO<sub>3</sub>)<sub>2</sub>), and magnesite (MgCO<sub>3</sub>), among other phases. However, the  
31 homogeneous nucleation and magnesite growth are slow at low temperatures (< 80 °C) relevant to  
32 geological conditions. The sluggish magnesite precipitation could be in part the consequence of  
33 the higher water-binding energies of magnesium(5,6) or the lattice limitation of carbonate on the  
34 geometrical configuration of CO<sub>3</sub> groups in magnesite(7).

35 Recently, magnesite precipitation was observed as the product of the reaction between synthetic  
36 and natural forsterite (Mg<sub>2</sub>SiO<sub>4</sub>), magnesium-rich end-member of olivine, and brucite (Mg(OH)<sub>2</sub>)  
37 with water-saturated supercritical CO<sub>2</sub> and at low temperatures(8–10). A common feature of all  
38 Me<sup>2+</sup>-bearing minerals is that once they contact wet supercritical CO<sub>2</sub>, a sub-nanometer water film

\*Corresponding author: [mjaq@uci.edu](mailto:mjaq@uci.edu)

39 forms on their surface that facilitate the formation of carbonic acid(11) and surface-metal  
40 complexes(12,13), and if the thickness of water film is above a threshold magnesite precipitation  
41 occurs(14–16). Time-resolved quantitative X-ray diffraction (XRD) experiments coupled with  
42 molecular dynamics simulations show that four water layers are required to allow Mg ion  
43 diffusivity across the water layers, enabling magnesite precipitation(16). Also, *In operando* XRD  
44 experiments on the surface of forsterite in contact with wet supercritical CO<sub>2</sub> at various  
45 temperatures revealed an anomalously low activation energy barrier for the formation  
46 magnesite(17). However, the underlying molecular mechanism of the carbonation reaction at the  
47 sub-nanometer olivine-water-CO<sub>2</sub> interface is puzzling due to experimental spatiotemporal  
48 limitations(12,18,19).

49 Indirect observations suggest that the lower dehydration energy of magnesium in the adsorbed  
50 water film is due to the presence of organic ligands(20)-(21) dissolved in CO<sub>2</sub> or the calcium-like  
51 water coordination shell of Mg<sup>2+</sup> in the adsorbed water nanofilm(17). However, the exact  
52 mechanism remains unknown. Molecular simulations promise to address this knowledge gap by  
53 providing an atomic-level insight into the physicochemical nature of the carbonation reaction at  
54 the olivine-water-CO<sub>2</sub> interface. First principle calculations offer promising avenues to explore  
55 chemical reactions at the nanoscale. For instance, quantum mechanical calculations indicate the  
56 H<sub>2</sub>O exchange promotes the dissolution of Mg-/Ca-silicate clusters(22). *Ab initio* thermodynamics  
57 simulations also show the partial hydroxylation of the most active forsterite surface cleavages  
58 when in contact with two monolayers of water at geologically relevant temperatures(23).

59 However, such quantum mechanical calculations become exorbitantly expensive when the number  
60 of atoms exceeds a few hundred. Furthermore, the dynamics of interfacial and bulk water are still  
61 not captured without uncertainty in these calculations due to complications in capturing dispersion  
62 effects. Force field (FF) methods can potentially address these issues and delve into the atomistic-  
63 level details reaching microseconds. Classical molecular dynamics (MD) simulations show that  
64 water adsorption on the forsterite surface is exothermic even at undersaturated high CO<sub>2</sub> pressures.  
65 They also confirm that CO<sub>2</sub> is displaced from the (010) forsterite surface by the adsorbed water  
66 molecules except at low water coverages(24). Raiteri et al.(25) have successfully developed a  
67 thermodynamically stable FF to model magnesium-(bi)carbonate ion pairing in the solution.  
68 Nevertheless, the current FFs for interfacial and bulk magnesium carbonate formation are  
69 nonreactive, i.e., they cannot simulate proton transfer processes and interfacial chemical reactions.  
70 Here, we attempt to develop a reactive FF to model carbonation reactions in bulk water and at the  
71 interface of magnesium-containing silicates and hydroxides.

72 This paper extends the current ReaxFF potential library to include magnesium interactions with  
73 oxygen, hydrogen, and carbon in an aqueous, bulk, and interfacial environment. The charge of  
74 magnesium is kept fixed, although the charge equilibration scheme in ReaxFF operates as usual  
75 for the rest of the elements. The geometrical and mechanical properties of a wide range of  
76 magnesium-containing crystals and magnesium-water binding energies are taken as observables  
77 in the fitting process. After completing the parameterization stage, we test the resulting parameters

78 for reproducing a group of magnesium-containing solids, water adsorption on crystal surfaces, and  
 79 Mg-(H)CO<sub>3</sub> ion pairing in the solution. Then, we explore our FF for some reactive environments,  
 80 including the proton transfer between bicarbonate and brucite surface, the free energy calculation  
 81 of the adsorption of carbonate on the forsterite surface, and carbonic acid dissociation in water in  
 82 the presence of magnesium ion.

## 83 2- Methods:

84 To describe molecular interactions in magnesium carbonate systems, we derive and validate a set  
 85 of potential parameters and merge the results with a previously-fitted ReaxFF forcefield(26) that  
 86 was applicable to aqueous and interfacial calcium carbonate systems. ReaxFF is a bond-order-  
 87 based FF that can simulate covalent bond formation and breakage. It also implements a charge  
 88 equilibration scheme that calculates atomic charges based on geometry and electronegativity.(27)  
 89 The total potential energy,  $E_{tot}$ , in ReaxFF is written as:

$$90 \quad E_{tot} = E_{bond} + E_{vdW} + E_{qeq} + E_{pen} + E_{over} + E_{under} + E_{val} + E_{tors} + E_{conj} \quad (1)$$

91 where  $E_{bond}$ ,  $E_{vdW}$ ,  $E_{qeq}$ ,  $E_{pen}$ ,  $E_{over}$ ,  $E_{under}$ ,  $E_{val}$ ,  $E_{tors}$ , and  $E_{conj}$  are respectively bonded, van  
 92 der Waals, coulombic, penalty, over-coordination, under-coordination, valence angle, torsion, and  
 93 conjugation energies. Like calcium, magnesium is present primarily as di-cation due to its ionic  
 94 nature, except for the case of shortly-lived univalent Mg<sup>+</sup> observed in the corrosion of magnesium  
 95 alloys(28). This allows us to incorporate a fixed magnesium charge and follow the recipe for the  
 96 fitting of ReaxFF for calcium carbonate systems that treat calcium charge fixed without any bond-  
 97 order consideration. To model electrostatics, we use the screened Coulomb potential between atom  
 98  $i$  and  $j$ , as implemented in REAXFF<sup>7</sup>:

$$99 \quad E_{coulomb} = Tap \cdot C \cdot \frac{q_i q_j}{[r_{ij}^3 + (1/\gamma_{ij})^3]^{1/3}} \quad (2)$$

100 where  $q_i$  and  $q_j$  are the charges of atoms  $i$  and  $j$  respectively, Tap is a 7<sup>th</sup> order polynomial taper  
 101 function that depends on the distance between the two atoms. This taper function ensures that  
 102 coulombic energy does not have discontinuity when charges enter or leave the cutoff radius of 10  
 103 Å.  $\gamma_{ij}$  is the pairwise screening parameter derived from the geometric mean of single atom  
 104 screening parameters  $\gamma_i$  and  $\gamma_j$ .

105 For the short-range repulsive Mg-C and Mg-H interactions, we choose the repulsive portion of  
 106 the Buckingham potential as follows:

$$107 \quad E_{ij} = A_{ij} e^{-r_{ij}/\rho_{ij}} \quad (3)$$

108 where  $A_{ij}$  and  $\rho_{ij}$  are characteristic energy and length, respectively. We also choose 12-6 Lennard-  
 109 Jones (LJ) potential for Mg-O interaction:

$$110 \quad E_{ij} = \frac{A_{ij}}{r^{12}} - \frac{B_{ij}}{r^6} \quad (4)$$

111 Where  $A_{ij}$  and  $B_{ij}$  are LJ fitting parameters. We note that in the reactive FF developed for the  
 112 calcium carbonate systems(26), only the repulsive part of the Lennard-Jones (12-6) potential was  
 113 chosen to describe the short-range interaction for Ca-O pairs based on the realistic assumption that  
 114  $\text{Ca}^{2+}$  have negligibly small electronic polarizability. However, in our fitting process, the attractive  
 115 part of the Lennard-Jones potential for Mg-O interactions helps achieve accurate magnesium  
 116 hydration energies and magnesium-water distance.

117 Atomic point charges are usually fixed in most classical MD frameworks, and therefore the effect  
 118 of the environment on the distribution of charges is neglected. However, in ReaxFF, a similar  
 119 approach to electronegativity equalization method (EEM) is used to update atomic charges at every  
 120 step based on the geometry and fitted atomic properties(29–32). In this method, total electrostatic  
 121 energy comprised of intra-atomic and interatomic potentials is defined as:

$$122 \quad E_{es}(q_1 \dots q_N, x_1 \dots x_N) = \sum_i (E_{i0} + \chi_i q_i + \frac{1}{2} J_i q_i^2) + \sum_i \sum_{j < i} q_i q_j J_{ij} \quad (5)$$

123 where  $x_i$  is the location of atom  $i$ ,  $q_i$  is its charge,  $E_{i0}$  is a zeroth-order constant,  $\chi_i$  is the  
 124 electronegativity,  $J_i$  is the self-coulomb repulsion in atom  $i$ , and  $J_{ij}$  is the Coloumb potential  
 125 between two unit charges located at  $x_i$  and  $x_j$ . The self-coulomb potential could be understood as  
 126 the electrostatic repulsion between two electrons in a doubly-occupied orbital. The first sum  
 127 represents the Taylor series expansion of the energy of an isolated atom up to the second order.  
 128 The second sum represents the conventional inter-atomic Coulomb potential between atoms  $i$  and  
 129  $j$  that is inversely proportional to their distance,  $|x_i - x_j|^{-1}$ .

130 The equilibrium charge distribution is achieved when the first derivatives of the total potential  
 131 with respect to each charge,  $\frac{\partial E_{es}}{\partial q_i}$  or chemical potentials, are all equal. Applying the constraint that  
 132 the total charge of the system is constant and using the Lagrange multiplier method leads to the  
 133 following linear equation:

$$134 \quad \sum_j M_{ij} q_j = \mu - \chi_i \quad (6)$$

135 where  $M_{ij}$  and  $\mu$  are respectively the coulomb-interaction matrix and the Lagrange's multiplier. If  
 136 some charges are fixed in the system, it is only required to construct the above matrix equation for  
 137 variable charges  $q_i$  while subtracting the inter-atomic Coulomb potential between the fixed charges  
 138 and unit charges at location  $x_i$  on the right-hand side.

139 To fit the FF parameters, namely Mg-C, Mg-H, Mg-O and  $\gamma_{Mg}$  potential parameters, we employ  
 140 the iterative fitting scheme that was previously used to fit the parameters of fixed-charge-calcium  
 141 REAXFF(26). To this end, we minimize the error function defined as the sum of squares of the  
 142 difference between experimental/DFT observable value and ReaxFF-calculated value:

$$143 \quad F = \sum_{i=1}^N w_i (f_i^{obs} - f_i^{calc})^2 \quad (7)$$

144 where  $f_i^{obs}$  is the experminetal/DFT-derived quantity,  $f_i^{calc}$  is the ReaxFF-calculated quantity,  $w_i$   
 145 is the weighting factor for the given quantity, and N is the number of observables. The selected

**Table 1.** The training dataset for parameterization of the forcefield.  $\text{MgC}_2$ ,  $\text{MgH}_2$ ,  $\text{MgO}$ ,  $\text{MgCO}_3$ , and  $\text{Mg}(\text{OH})_2$  are crystal structures.  $\text{Mg}^{2+}[\text{H}_2\text{O}]_6$  and  $\text{Mg}^{2+}[\text{H}_2\text{O}]_6[\text{H}_2\text{O}]_2$  are magnesium-water clusters consisting first and second shell of waters, respectively. Magnesium-water clusters are only used to fit the aqueous forcefield, while crystal structures are used for both aqueous and interfacial forcefields. The Mg-O-O angles are the angles between water and magnesium in the first and second hydration shells.

structure	lattice constants	atomic configuration	bulk modulus	bond distance	angle value	hydration energy
$\text{MgC}_2$	x	x				
$\text{MgH}_2$	x	x	x			
$\text{MgO}$	x	x	x			
$\text{MgCO}_3$	x	x	x			
$\text{Mg}(\text{OH})_2$	x	x	x			
$\text{Mg}^{2+}[\text{H}_2\text{O}]_6$				Mg-Ow	Mg-Ow-Ow	x
$\text{Mg}^{2+}[\text{H}_2\text{O}]_6[\text{H}_2\text{O}]_2$				Mg-Ow	Mg-Ow-Ow	x

146 observables are the solid lattice constants, atomic configurations, bond/angle values, and bulk  
147 modulus for some of the crystals selected for fitting, as shown in **Table 1**.

148 In each iteration, first the Mg-H and Mg-C parameters are fitted to the lattice structure of  
149  $\alpha\text{MgH}_2$ (33), and  $\text{MgC}_2$  (34) and the bulk modulus of  $\alpha\text{MgH}_2$ . Then, the derived Mg-H and Mg-C  
150 parameters are used to fit Mg-O and  $\gamma_{\text{Mg}}$  using the lattice structure and the bulk modulus of  
151  $\text{Mg}(\text{OH})_2$ (35,36),  $\text{MgO}$ (37), and  $\text{MgCO}_3$ (38,39) crystals along with the total hydration energies  
152 ( $E_{\text{hyd}}$ ) of water molecules on the first and second shell(40) of  $\text{Mg}^{2+}$ , namely  $[\text{Mg}(\text{H}_2\text{O})_6]^{2+}$  and  
153  $[\text{Mg}(\text{H}_2\text{O})_6](\text{H}_2\text{O})^{2+}$ . Note that the Mg-H and Mg-C parameters are kept fixed at this step. Also,  
154 the Mg-Ow bond length of the first shell of water molecules and some of the Mg-Ow-Ow angles  
155 were taken as fitting observables, in which Ow being the oxygen in the water in the first and second  
156 shell. We repeat these two steps iteratively until we obtain a satisfactory parameter set.

157 Based on water adsorption calculation on crystal surfaces described later, assigning a formal  
158 charge of +2 to magnesium atoms causes an overestimation of water adsorption energies compared  
159 to density functional theory (DFT) calculations. Since electrostatics contributions play a  
160 significant role in water adsorption energies on crystal surfaces, we decided to parameterize two  
161 separate force fields: 1) The aqueous FF with magnesium charge fixed to +2, which is suitable for  
162 aqueous magnesium carbonate systems, and 2) The interfacial FF, for which we fit the magnesium  
163 charge to the geometrical and mechanical properties of magnesium-containing solids and can be  
164 used for crystalline solids and their interfaces with water. Note that we only used the Mg-water  
165 cluster to fit the aqueous FF and not the interfacial FF. Also, the charge of magnesium in the  
166 interfacial FF is fitted in the second step of each iteration.

167 Magnesium-water clusters are simulated using the Gaussian16 code(41). B3LYP exchange-  
168 correlation functional(42,43) is used with the large 6-311++G(2d,2p) basis set. Berny optimization  
169 method(44) is used with the Tight option and Ultrafine integration grid(45) to ensure convergency  
170 is reached for clusters with soft degrees of freedom. Dispersion correction is applied using the  
171 DFT-D3 method of Grimme(46,47).

172 To calculate surface hydration energies, we implement Vienna Ab-initio Simulation Package  
173 (VASP)(48). Projector augmented wave (PAW) potentials(49) are used with the kinetic cut-off  
174 energy of 520 eV. The Perdew-Burke-Ernzerhof (PBE) generalized gradient approximation  
175 (GGA) is used as the exchange-correlation functional(50). Also, van-der-Waals dispersion forces  
176 are considered using the DFT-D3 method of Grimme. For the crystal surfaces, 2x2x1 mesh points  
177 are used to sample the K-space using Monkhorst-Pack scheme. Conjugate gradient method is used  
178 for geometry optimization. For simplicity, we refer to the DFT methods used for cluster and  
179 surface calculations as B3LYP-D3 and PBE-D3 respectively.

**Table 2.** Fitted interatomic potential parameters to be incorporated with REAXFF. The Mg-H and Mg-C interactions are modelled with Buckingham potential (eq 3) and the Mg-O interaction is modelled with Lennard-Jones (LJ) 12-6 potential (eq 4). Gamma is the screening parameter used in Coulombic interaction according to eq. 2.

Interaction	Aqueous Forcefield						Interfacial Forcefield					
	$q_{Mg}$	$\gamma$ ( $\text{\AA}^{-1}$ )	$A_{ij}(\text{ev}.\text{\AA}^{12})$	$B_{ij}(\text{ev}.\text{\AA}^6)$	$A_{\text{buck}}(\text{ev})$	$\rho_{\text{buck}}(\text{\AA})$	$q_{Mg}$	$\gamma$ ( $\text{\AA}^{-1}$ )	$A_{ij}(\text{ev}.\text{\AA}^{12})$	$B_{ij}(\text{ev}.\text{\AA}^6)$	$A_{\text{buck}}(\text{ev})$	$\rho_{\text{buck}}(\text{\AA})$
Mg Coulomb	2.00	0.55	-	-	-	-	1.284 6	0.5298	-	-	-	-
Mg-H	-	-	-	-	293.366	0.289894	-	-	-	246.154	0.2572	-
Mg-C	-	-	-	-	320.9	0.37	-	-	-	240.6954	0.3228	-
Mg-O	-	-	3704.1911	44.480255	-	-	-	-	53.5115	-	-	-



**Table 3.** Water binding energies (eV) calculated for  $[\text{Mg}(\text{H}_2\text{O})_n](\text{H}_2\text{O})_m^{2+}$ . n and m refer to the number of water molecules in the first and second shell respectively. Hydration energy ( $E_{\text{hyd}}$ ), binding energy ( $E_{\text{bind}}$ ), and successive ( $\Delta E$ ) binding energy are calculated based on Eqs. 8, 9, and 10, respectively.

Cluster	$E_{\text{hyd}}$ ReaxFF (aq) (eV)	$E_{\text{bind}}$ ReaxFF (aq) (eV)	$\Delta E$ ReaxFF (aq) (eV)	$E_{\text{hyd}}$ ReaxFF (int) (eV)	$E_{\text{bind}}$ ReaxFF (int) (eV)	$\Delta E$ ReaxFF (int) (eV)	$E_{\text{hyd}}$ B3LYP-D3 (eV)	$E_{\text{bind}}$ B3LYP-D3 (eV)	$\Delta E$ B3LYP-D3 (eV)	$E_{\text{bind}}$ B3LYP <sup>a</sup> (eV)	$\Delta E$ B3LYP <sup>a</sup> (eV)	$E_{\text{bind}}$ Non- Reactive FF (eV)	$\Delta E$ Non- Reactive FF(eV)
n = 2, m = 0	-5.42	-5.67		-3.21	-3.47		-6.59	-6.83		-6.61		-4.76 <sup>d</sup> , -5.95 <sup>e</sup>	
n = 3, m = 0	-7.49	-8.08	-2.41	-4.33	-4.92	-1.45	-8.66	-9.43	-2.59	-9.00	-2.39	-6.93 <sup>d</sup> , -8.15 <sup>e</sup>	-2.17 <sup>d</sup> , - 2.77 <sup>e</sup>
n = 4, m = 0	-9.47	-10.15	-2.07	-5.43	-6.13	-1.21	-10.47	-11.53	-2.11	-10.90	-1.90	-8.92 <sup>d</sup> , -9.97 <sup>e</sup>	-1.98 <sup>d</sup> , - 2.44 <sup>e</sup>
n = 5, m = 0	-10.15	-11.57	-1.41	-5.43	-6.84	-0.71	-11.29	-13.02	-1.49	-12.11	-1.21	-10.34 <sup>d</sup> , -11.2 <sup>e</sup>	-1.42 <sup>d</sup> , - 1.57 <sup>e</sup>
n = 6, m = 0	-10.98	-12.84	-1.27	-5.60	-7.46	-0.62	-12.10	-14.39	-1.37	-13.18	-1.06	-11.77 <sup>d</sup> , -12.22 <sup>e</sup>	-1.43 <sup>d</sup> , - 1.52 <sup>e</sup>
n = 6, m = 1 <sup>b</sup>	-11.68	-14.05	-1.21	-6.51	-8.03	-0.56	-12.55	-15.32	-0.92	-13.96	-0.78		
n = 6, m = 1 <sup>c</sup>	-11.64	-14.01	-1.17	-6.60	-8.12	-0.65	-12.62	-15.38	-0.98	-14.00	-0.82	-12.6 <sup>d</sup> , -12.64 <sup>e</sup>	-0.83 <sup>d</sup> , - 0.93 <sup>e</sup>
n = 6, m = 2	-12.09	-15.03	-1.02	-5.80	-8.74	-0.62	-13.21	-16.22	-0.84	-14.62	-0.66	-13.31 <sup>d</sup> , -12.93 <sup>e</sup>	-0.71 <sup>d</sup> , - 1.06 <sup>e</sup>

<sup>a</sup> From <sup>39</sup>. <sup>b</sup> one hydrogen bond. <sup>c</sup> two hydrogen bonds. <sup>d</sup> core-shell potential[24] <sup>e</sup> Thermodynamically consistent potential[25]. (aq) refers to aqueous and (int) refers to interfacial forcefields.

### 182 3- Results and Discussions:

#### 183 3-1 Solvation Structures and

184 **Energies:** The final fitted parameters  
 185 derived according to the procedure  
 186 described in the Methods section are  
 187 presented in **Table 2**. These parameters  
 188 should accompany the ReaxFF library  
 189 provided in the **Supporting**  
 190 **Information**. The hydration energies of  
 191 magnesium are calculated for clusters up  
 192 to eight water molecules, as shown in  
 193 **Table 3 and Fig. 1**. The total hydration  
 194 energy,  $E_{hyd}$ , the binding energy,  $E_{bind}$ ,  
 195 and the difference in the energies if one  
 196 water molecule was added to the cluster,  
 197  $\Delta E$ , are calculated based on the  
 198 following relationships:

199

200

201

202

$$203 \quad E_{hyd} = E\{Mg(H_2O)_n^{2+}\} - E\{(H_2O)_n\} - E(Mg^{2+}) \quad (8)$$

$$204 \quad E_{bind} = E\{Mg(H_2O)_n^{2+}\} - nE\{(H_2O)\} - E(Mg^{2+}) \quad (9)$$

$$205 \quad \Delta E = E\{Mg(H_2O)_n^{2+}\} - E(H_2O) - E\{Mg(H_2O)_{n-1}^{2+}\} \quad (10)$$

206 The difference between total hydration energy and binding energy is that the energy of a cluster of  
 207 water molecules is used in the hydration energy while the energy of a single water molecule is  
 208 used in the calculation of binding energies. The dispersion correction used in our B3LYP-D3  
 209 calculations can affect the water cluster energies. The magnitude of  
 210 the binding energies ( $E_{bind}$ )  
 211 calculated from our B3LYP-D3  
 212 calculations are larger than those  
 213 previously calculated from B3LYP  
 214 calculations(5) without dispersion  
 215 corrections. The discrepancy in  
 216 binding energies is expected when  
 217

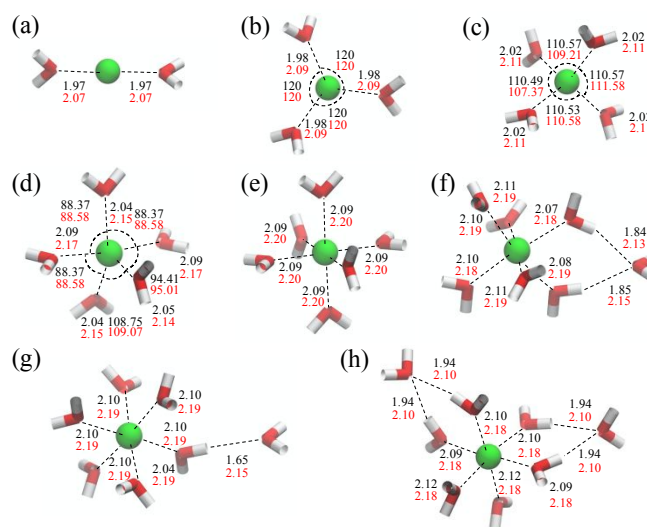


**Figure 1.**  $Mg^{2+}$ -water clusters. a)  $Mg^{2+}(H_2O)_2$  b)  $Mg^{2+}(H_2O)_3$  c)  $Mg^{2+}(H_2O)_4$  d)  $Mg^{2+}(H_2O)_5$  e)  $Mg^{2+}(H_2O)_6$  f)  $Mg^{2+}(H_2O)_6(H_2O)$  The water molecule in the second shell has one hydrogen bond with a first-shell water molecule g)  $Mg^{2+}-(H_2O)_6(H_2O)$ . The water molecule in the second shell has two hydrogen bonds with two first-shell water molecules h)  $Mg^{2+}-(H_2O)_6(H_2O)_2$ . The black and red values respectively refer to B3LYP-D3 and ReaxFF calculations. Mg atoms are shown by green balls, and water oxygen and hydrogen atoms are colored as red and white sticks, respectively.

**Table 4.** Bond distances between  $Mg^{2+}$  and water oxygen derived from ReaxFF and DFT in  $[Mg(H_2O)_n]^{2+}$  clusters.

Cluster	Mg-Ow (Å) ReaxFF	Mg-Ow (Å) B3LYP-D3	Mg-Ow (Å) B3LYP*
n = 2	2.07	1.95	1.95
n = 3	2.09	1.97	1.97
n = 4	2.11	2.02	1.99
n = 5	2.15, 2.17	2.04, 2.09	2.03, 2.07
n=6	2.20	2.09	2.08

\* From <sup>39</sup>.

**Table 5.** Lattice properties and bulk modulus for magnesium containing crystals calculated from two fitted ReaxFF forcefields, compared to experiments.

Crystal Formula	Aqueous forcefield			Interfacial forcefield			a (Å)- exp.	c (Å)- exp.	K (GPa)- exp
	a (Å)	c (Å)	K (GPa)	a (Å)	c (Å)	K (GPa)			
Brucite	12.17	14.42	60	12.35	12.85	73	12.57	14.3	46
Magnesia	8.62			8.96			8.94		
Magnesite	5.94	17.83	163	6.11	18.36	105.18	5.67	17.02	110
Magnesium Hydride	18.69	15.25	58.8	18.69	15.77	21	17.94	15	51
Magnesium Carbide	16.78	15.71		17.22	14.92		15.74	15.06	
Nesquehonite	22.52	24.25		23.39	24.22		23.10	24.25	
Dolomite	24.57	6.14		25.00	6.25	96	24.05	6.013	94
Diopside	12.87	15.95		13.17	15.87		13.20	15.75	

218 we use dispersion correction that was shown to more accurately capture van der Waals interactions  
 219 and hydrogen bonding(51–53).  $|\Delta E|$  reduces as the number of water molecules increases in  
 220 ReaxFF and DFT. Also, as the number of water molecules increases, the error in ReaxFF hydration  
 221 energies compared to DFT results reduces. This is due in parts to the charge equalization scheme  
 222 in ReaxFF that tends to uniformly distribute charges, therefore working better for larger clusters  
 223 where charges are less localized.

224 We also provide in **Table 3** the binding energies resulted from two known non-reactive potentials.  
 225 One is the core-shell potential developed by Kerisit and Parker(54), which is successfully used to  
 226 study the free energy of metal cation (Sr, Mg, Ca) adsorption on the surface of calcium carbonate  
 227 crystal. The other is the thermodynamically consistent forcefield developed by Raiteri et al.(25) to  
 228 model alkaline-earth carbonates in water.

229 As reported in Table 3, our reactive forcefield gives more accurate results than both non-reactive  
 230 forcefields for the binding energies of clusters with equal or more than 4 water molecules. This  
 231 roots back in the charge equalization method implemented in our forcefield that does not perform  
 232 accurately for localized charges, whereas for the systems with more distributed charges it is shown  
 233 to be more reliable. The energy difference in binding energies ( $\Delta E$ ) are captured well through both  
 234 reactive and the non-reactive forcefields especially when we add water molecules to the first shell  
 235 of magnesium. When we add water to the second shell, although binding energies calculated from  
 236 our reactive forcefield are within a good range of binding energies calculated from DFT-D3, we  
 237 observe larger discrepancy in  $\Delta E$ . This can be the result of limited charge screening in our  
 238 forcefield due to the fixed magnesium charge. Same is true for the Raiteri et al.'s forcefield with  
 239 fixed charges, whereas the Kerisit and Parker's forcefield is more consistent in calculating  $\Delta E$ , due  
 240 to the polarizability of water molecules provided by the core-shell model. Also, we report the  
 241 hydration and binding energies of magnesium-water cluster calculated from our interfacial  
 242 forcefield in **Table 3**. As shown in the table, the interfacial reactive forcefield gives much less  
 243 accurate results when compared to the aqueous ReaxFF due to the smaller Mg charge.

244 The distance between  $Mg^{2+}$  and water oxygens in  $Mg(H_2O)_n^{2+}$  as obtained from ReaxFF, our DFT  
245 simulations, and a previous DFT work(5) are presented in **Table 4**. Our B3LYP-D3 calculations  
246 show slightly larger bond lengths between magnesium and the water oxygens compared to  
247 previous B3LYP calculations. Similar overestimations were observed for the  $Na^+$ -water bond  
248 lengths when dispersion correction was implemented(55). On the other hand, ReaxFF gives  
249 acceptable bond distance values, although in general overestimates them. The Mg-Ow bond  
250 lengths increase as the number of water molecules increases, in agreement with DFT results.

251 **3-2: Crystal structures:** The resulting fitted parameters are used to calculate the lattice properties  
252 and bulk moduli of a list of magnesium-containing solid phases, as shown in **Table 5**. Along with  
253 the crystals used in the fitting procedure, few other crystal structures are selected to evaluate the  
254 transferability of the derived FF beyond the geometrical and mechanical observables used in the  
255 parameterization process. Here, we present the calculated crystal structures based on both aqueous  
256 and interfacial FF to show the impact of setting magnesium charge to a value less than +2 as  
257 expected for covalent-ionic systems.

258 As shown in **Table 5**, magnesite lattice parameters are reproduced with acceptable accuracy with  
259 both forcefields compared to experimental results. However, the bulk modulus is best captured  
260 with the interfacial FF with an underestimation of about 9%, while the aqueous FF produces poor  
261 results. The elastic constant,  $C_{11}$ , is calculated to be 168 GPa for magnesite according to our  
262 interfacial FF, which is reasonable compared to DFT calculations with GGA functional. However,  
263 it deviates from the DFT-LDA results overall gives better results when compared to  
264 experiments(56). Surprisingly, the elastic constants in the ab plane,  $C_{12}$ , and  $C_{13}$ , are very  
265 accurately calculated compared to DFT-LDA and experiments. However,  $C_{11}+C_{12}$  differs a lot  
266 from the experimental value of 334 GPa(56). Also,  $C_{33}$  is calculated to be 165 GPa compared to  
267 the experimental value of 156 GPa. We note that our reactive interfacial FF gives reasonable results  
268 for the mechanical properties of magnesite when compared to the non-reactive thermodynamically  
269 consistent FF(25) that cannot properly capture the bulk modulus. It can be attributed to the choice  
270 of the magnesium charge that is taken less than +2.

271 The structure and mechanical properties of dolomite which were not part of the training set are  
272 calculated, and the results are shown in **Table 5**. Calcium parameters are taken from a previously  
273 fitted reactive FF for aqueous calcium carbonate systems with a fixed calcium charge of 2.(26)  
274 Compared to experimental values, the lattice parameters are overestimated by about 4% and 2%,  
275 respectively, for the interfacial and aqueous forcefields(57). Based on the interfacial forcefield, the  
276 calculated bulk modulus is 96 GPa based on Voigt definition, slightly overestimating the  
277 experimental value of 94 GPa(58). The aqueous FF gives poor results when it comes to the  
278 mechanical properties of dolomite. Based on our interfacial FF, the  $C_{11}$  constant is 183 GPa  
279 compared to 204 GPa based on Brillouin zone spectroscopy measurements(59). Also, the  
280 calculated  $C_{33}$  constant is 96 GPa agrees well with the experimental value of 97 GPa. However,  
281 the rest of the elastic constants that are calculated by our forcefields are less accurate.

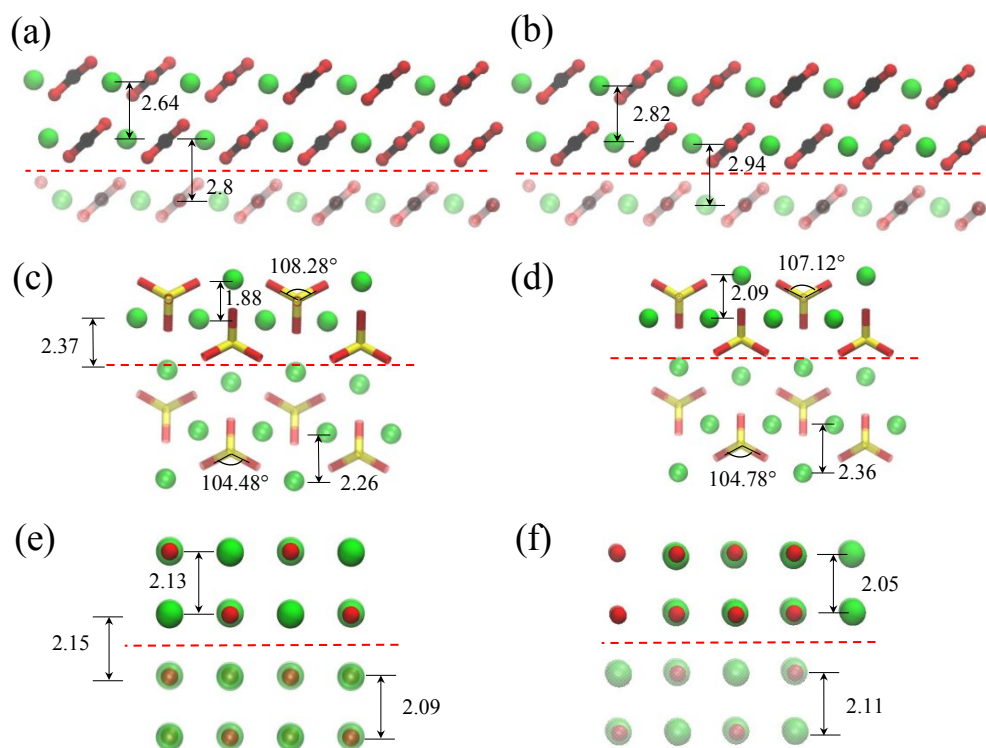


**Figure 2.** The dry surface of magnesite, forsterite, and magnesia. a) The dry  $(10\bar{1}4)$  surface of magnesite calculated from PBE-D3. The distance between magnesium layers in the bulk phase is 2.77 Å. b) The dry  $(10\bar{1}4)$  surface of magnesite as calculated with ReaxFF. The distance between magnesium layers in the bulk phase is 2.80 Å. c) The dry  $(010)$  surface of forsterite calculated from PBE-D3. d) The dry  $(010)$  surface of forsterite calculated from ReaxFF. e) The dry  $(100)$  surface of magnesia (MgO) calculated from PBE-D3. f) The dry  $(100)$  surface of magnesia (MgO) calculated from ReaxFF. The black and red values refer to PBE-D3 and ReaxFF calculations, respectively. The atoms below red dashed lines are fixed, while the top atoms are able to move. Magnesium, carbon, oxygen and silicon colored as green, black, red and yellow, respectively. Distances are in Angstroms.

282 The rest of the solid phases in **Table 5** are reasonably reproduced with both aqueous and interfacial  
 283 forcefields in terms of lattice constants. Interestingly, brucite lattice constants are better captured  
 284 with the aqueous FF. Especially in the  $c$  direction where the structure is layered, the lattice constant  
 285 is only 1% deviating from the experiment, compared to the 10% underestimation of the interfacial  
 286 FF. This discrepancy can be explained by the lower Mg-Ow bond lengths in the magnesium-water  
 287 clusters used in the parameterization of the aqueous FF.

288 **3-3 Surface hydration:** The interaction of water with metal-containing rocks is crucial to  
 289 understand  $\text{CO}_2$  sequestration(60), electrochemical reactions(61), and accretion of the Earth from  
 290 the water adsorption on dust grains(62,63), etc. However, our knowledge of the mineral-water  
 291 interface is limited due to experimental and theoretical difficulties. Here, we select three crystals,  
 292 namely forsterite, magnesite, and magnesium oxide, to examine the fitted FF to predict the  
 293 geometric structure of dry and hydrated surfaces. We use  $(010)$  cleaved surface of forsterite which  
 294 was previously shown to have the lowest surface energy(64). For magnesite, we choose the  $(10\bar{1}$

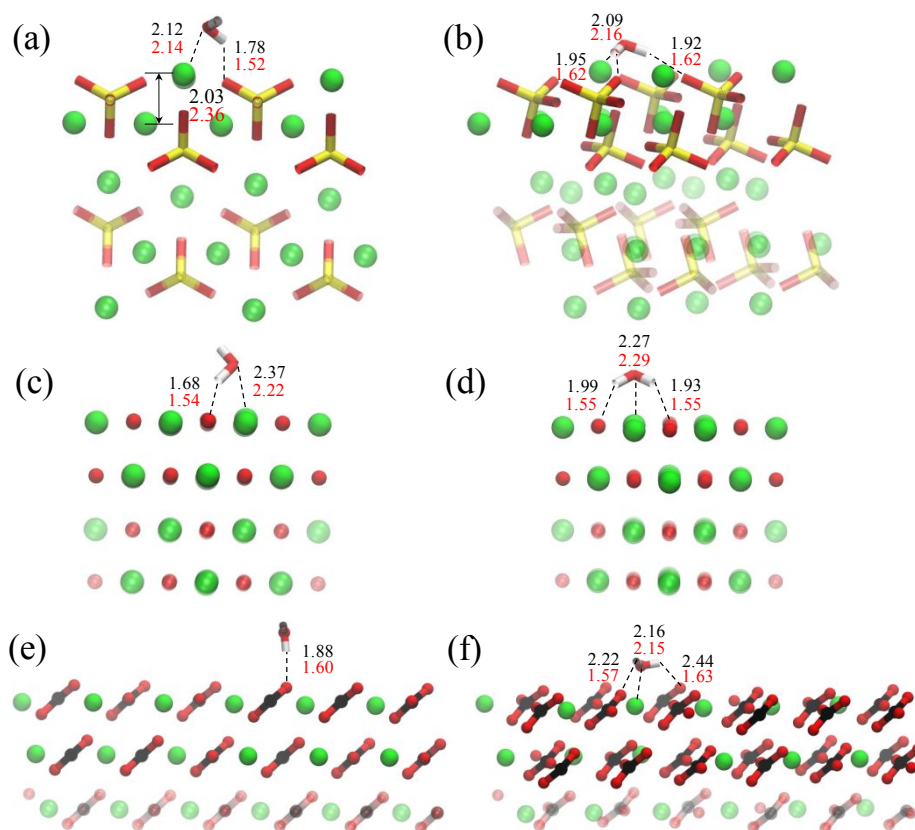


**Figure 3.** The hydrated surface of magnesite, forsterite, and magnesia. The adsorption of water on the (010) surface of forsterite with a) side and b) flat configurations. The adsorption of water on the (100) surface of magnesia with c) side and d) flat configurations. The adsorption of water on the (10 $\bar{1}$ 4) surface of magnesite with e) side and f) flat configurations. The transparent atoms are held fixed during the simulation, while the rest of the atoms are free to move. Magnesium, carbon, oxygen and silicon colored as green, black, red and yellow, respectively. The distance values in black and red are derived from PBE-D3 and ReaxFF. Distances are in Angstroms.

295 4) surface cleavage that is shown by scanning electron microscopy analyses to be the dominant  
 296 surface(65). For MgO, we choose the (001) surface. Only the top two layers of magnesium in all  
 297 crystals are allowed to move while fixing the bottom layers to represent the bulk-like crystals.

298 The dry surfaces are relaxed using DFT and the interfacial reactive forcefield, as shown in **Fig. 2.**  
 299 **a-f.** On the forsterite surface, the top magnesium layer displaces toward the bulk phase for about  
 300 0.26 Å and 0.29 Å using DFT and ReaxFF, respectively. This results from the fact that the surface  
 301 magnesium is undercoordinated and is attracted toward the negatively charged oxygens in the  
 302 bottom layer. Also, the second top magnesium layer displaces slightly toward the surface for about  
 303 0.11 Å and 0.02 Å using DFT and ReaxFF, respectively. ClayFF, a classical FF with fixed charges,  
 304 shows a displacement of 0.34 Å toward the bulk phase and 0.05 Å toward the surface for the first  
 305 and second magnesium layers. The top silicon atoms move upward for about 0.19 Å, and the  
 306 oxygen-silicon-oxygen angle changes from 104.48° to 108.28°. Using ReaxFF, the top silicon  
 307 atoms move outward for about 0.07 Å, and the angle changes from 104.78° to 107.12°. This results  
 308 from the lower equilibrium bond distance between undercoordinated magnesium and silicate  
 309 oxygens. Also, the angle change can significantly reduce the stability of surface silicate groups

310 and can potentially give rise to the production of carbonate groups when CO<sub>2</sub> is in the surface  
311 vicinity. DFT results are in close agreement with a previously reported DFT work(66) that used  
312 D2 dispersion correction.

313 The surface features of carbonate minerals like calcite, magnesite, and dolomite are important for  
314 modeling the dissolution/precipitation processes in the geological carbon cycle. Magnesite and  
315 dolomite surface reactivity has been investigated experimentally using surface complexation  
316 models(65,67). However, reactive molecular simulations are yet applied to study these problems.  
317 According to our calculations on the magnesite's dry surface, slight displacement is found on the  
318 (10 $\bar{1}$ 4) surface, compared to Calcite (CaCO<sub>3</sub>) which has a lower bulk modulus of about 73.5  
319 GPa(68). Upon DFT calculations, the first magnesium layer moves toward the bulk phase by about  
320 0.11 Å, and the second magnesium layer moves away from it by 0.03 Å. With ReaxFF, the first  
321 magnesium layer moves toward the inner layers by about 0.1 Å, and the second magnesium layer  
322 moves away from the bulk phase by 0.02 Å, in full agreement with the DFT calculations. The CO<sub>3</sub>  
323 also distorts slightly like akin to the observations in the DFT simulations.

324 We also test our FF to reproduce the MgO (001) surface. MgO has critical industrial applications  
325 such as heterogeneous catalysis and concrete construction(69–71). Based on our calculation, the  
326 anhydrous (001) surface of MgO changes only slightly. Based on our DFT calculations, we  
327 observe that the first magnesium layer displaces 0.16 Å out of the surface, while the second layer  
328 displaces only for 0.06 Å. Our ReaxFF simulations underestimate the displacement of the first and  
329 second magnesium layers by 0.09 Å and 0.05 Å, respectively.

330 After relaxing the dry surfaces, we add a water molecule on top of crystal surfaces and relax them  
331 using PBE-D3 and ReaxFF. Two configurations of water are found on each crystal surface, as  
332 shown in **Fig. 3. a-f** without dissociating. On the forsterite (010) surface, a water molecule can  
333 either donate a hydrogen bond to a onefold coordinated silicate oxygen or donate two bonds to two  
334 onefold coordinated silicate oxygen as shown, respectively in **Fig. 3. a** and **Fig. 3. b**. We call the  
335 former case “side water” and the latter case “flat water”. In both cases, the water oxygen is found  
336 coordinated around a surface magnesium. The adsorption energy based on PBE-D3 calculations  
337 for the “side water” and the “flat water” are respectively -0.90 eV and -1.34 eV. The calculated  
338 adsorption energies are less exothermic than those calculated through DFT with D2 dispersion  
339 correction, which produced -1.48 eV and -1.42 eV for “flat water” and “side water” configurations,  
340 respectively(66).

341 The adsorption energies for the “flat water” and “side water” configurations based on ReaxFF are  
342 -2.38 eV and -1.6 eV, respectively. The aqueous FF gives even worse predictions about twice the  
343 amount for the interfacial FF, although the former gives accurate hydration energies of solvated  
344 magnesium in water. Although assigning a charge less than +2 to the less ionic magnesium in the  
345 crystal partially resolves this problem, we believe that the observed difference in water adsorption  
346 energies between PBE-D3 and ReaxFF roots in the hydration of silicate groups. The lower ReaxFF  
347 hydroxylation energy of water on silicates compared to DFT calculations(72) support the evidence.



348 This discrepancy can be alleviated by further improving ReaxFF's Si/O/H parameter set to include  
349 water geometry and adsorption energy on silicates.

350 For the case of "side water," surface magnesium is displaced away from the surface by 0.45 Å and  
351 0.27 Å calculated from PBE-D3 and ReaxFF, respectively, most probably due to the charge  
352 transfer caused by the water molecule. Using interfacial ReaxFF, the length of the donated  
353 hydrogen bond for the "flat water" is underestimated by about 0.3 Å compared to our PBE-D3  
354 results. Also, the bond between surface magnesium and the water oxygen is overestimated by  
355 about 0.02 Å and 0.07 Å for the "side water" and "flat water," respectively, using the interfacial  
356 reactive FF compared to the PBE-D3 simulations. This difference is due to the overestimated  
357 magnesium-water bond distance in our parameterization. The donated hydrogen bond in the "side  
358 water" configuration is 0.2 Å shorter in ReaxFF compared to PBE-D3. However, the magnesium  
359 water distance, in this case, is only 0.02 Å overestimated with ReaxFF compared to DFT.

360 Similar to the forsterite surface, the hydrogen bonds on the MgO surface are shorter when modeled  
361 with ReaxFF compared to PBE-D3, as shown in **Fig. 3. c-d**. The hydrogen bond formed between  
362 the water hydrogen and the undercoordinated oxygen on the surface is 1.54 Å resulted from  
363 ReaxFF, compared to the 1.68 Å calculated via PBE-D3. Contrary to forsterite cases, the  
364 magnesium-water distance on MgO surface is underestimated by ~0.15 Å. Also, the hydrogen  
365 bonds of the "flat water" case are shorter by almost ~0.45 Å in ReaxFF compared to PBE-D3  
366 values, although the magnesium oxygen bond is properly calculated. This shows that the water  
367 dipole moment is more oriented toward the surface in ReaxFF. According to our energy  
368 calculations at 0 K, the structure of "side water" is more stable than "flat water" opposite to the  
369 forsterite adsorption cases. The adsorption energies derived using PBE-D3 are -0.42 eV and -0.48  
370 eV for "flat water" and "side water", respectively. Similar to the forsterite surface, the adsorption  
371 energies from interfacial ReaxFF are more exothermic than adsorption energies resulted from  
372 PBE-D3 by -1.38 eV and -1.70 eV.

373 On the surface of Magnesite, the adsorption energies for the "flat water" and "side water" with  
374 PBE-D3 are -0.64 eV and -0.19 eV, respectively. However, ReaxFF-derived adsorption energies  
375 for "flat water" and "side water" are -1.55 eV and -0.48 eV overestimating their magnitude  
376 compared to their corresponding values from PBE-D3 calculations. The magnesium distance to  
377 the water oxygen simulated from ReaxFF is close to its value from PBE-D3, although the hydrogen  
378 bond distances are smaller in ReaxFF than PBE-D3.



379 Moving away from the single  
 380 water adsorption, we examine the  
 381 cases where 1 to 5 monolayers of  
 382 water exist on the (010) surface of  
 383 forsterite. In the corresponding  
 384 ReaxFF simulations, all the one-  
 385 folded silicate oxygen atoms  
 386 become hydrated. Moreover,  
 387 previous DFT simulations of the  
 388 (100) surface of MgO have  
 389 shown that a complete monolayer  
 390 of water hydroxylates the  
 391 surface(73). We calculate the  
 392 adsorption energy for various  
 393 monolayers on the surface of  
 394 forsterite, as demonstrated in **Fig.**  
 395 **4.** Since the adsorption energy of  
 396 the first monolayer was

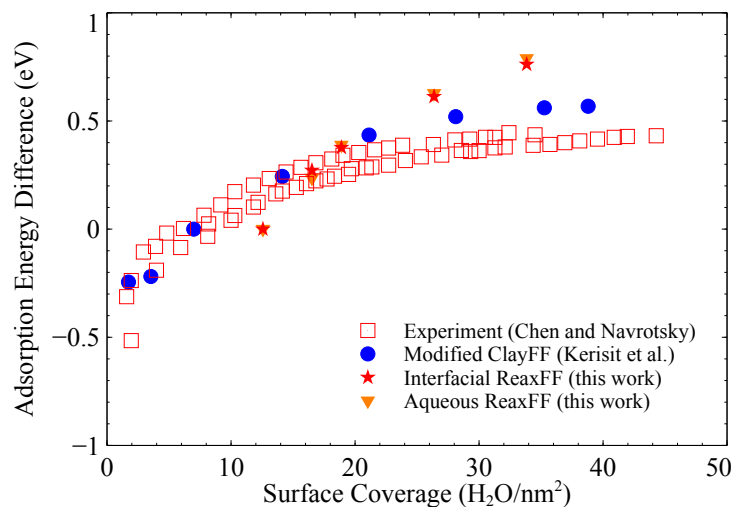


**Figure 4.** The monolayer water adsorption energy difference on the surface of forsterite from simulations and experiments. The energy difference refers to the adsorption energy of  $n$  monolayers of water subtracted by the adsorption energy of one monolayer water ( $n=2,3,4,5$ ).

397 substantially high due to interactions with the silicates, we only present the difference in the  
 398 adsorption energy of  $n$  water monolayers ( $n=2,3,4,5$ ) and the adsorption energy of one monolayer.  
 399 Comparison with experiment and modified ClayFF potential(24), a non-reactive forcefield, shows  
 400 that two and three monolayers of water give the best adsorption energies when subtracted from the  
 401 adsorption energy of a single monolayer, and it is in an acceptable experimental range when four  
 402 and five monolayers are present on the surface.

403 **3-4 Ion Pairing:** The formation of  $\text{MgCO}_3$  and  $[\text{MgHCO}_3]^+$  ion pairs in the solution is a precursor  
 404 for the nucleation of magnesium carbonate(74,75). However, the molecular mechanism that leads  
 405 to the nucleation and growth of crystalline or amorphous magnesium carbonate phases at different  
 406 thermodynamic conditions and thin water films is not known(8,9,17,75,76). Also, the attachment  
 407 of carbonate to the surface magnesium on crystals like forsterite can lead to dissolution, known as  
 408 ligand-promoted mineral dissolution(77). Therefore, studying the energetics of the pairing  
 409 reactions becomes crucial to understand homogeneous and heterogeneous nucleation and  
 410 growth(13).

411 Here, we examine the fitted aqueous FF to model the structure of the separated ions (SI), solvent  
 412 separated ion pairs (SSIP), and contact ion pairs (CIP) and their relative potential energy. We use  
 413 recent geometries(12) calculated by DFT for hydrated  $\text{Mg}^{2+}$  and  $\text{HCO}_3^-/\text{CO}_3^{2-}$  in SI, SSIP, and CIP  
 414 form as initial structures and relax them using energy minimization with our aqueous reactive FF.  
 415 The resulting structures are shown in **Fig. 5. a-d**. The relative energies between SSIP and CIP  
 416 structures from our reactive simulations are compared to MP2/aD level and B3LYP/aD level  
 417 calculations(12) in **Table 6**. As shown, the relative energies derived from our FF are within the  
 418 acceptable range of the DFT results. However, SSIP structures are more stable than CIP contrary

419 to the DFT results and infrared  
 420 spectroscopic measurements in the  
 421 solution(78). Nevertheless,  
 422 nucleation either takes place in the  
 423 solution or at the mineral-water  
 424 interface. Therefore, it is essential to  
 425 test the FF in the solution and  
 426 measure the relative stability of SSIP  
 427 and CIP structures.

428 To this end, we construct a cubic box  
 429 containing 560 water molecules and  
 430 run MD at 298.15 K. First, we relax  
 431 the cell in constant isobaric  
 432 isothermal ensemble (NPT) using the  
 433 Nose-Hoover thermostat and barostat  
 434 with 0.5 fs timestep and relaxation  
 435 time of 10 fs. Upon convergence in  
 436 the box dimensions, we relax the  
 437 system in canonical ensemble (NVT) at 298.15 K. Then, we place one magnesium ion and one  
 438 carbonate ion at some distance in the solution and run MD for 6 ns. We observe that the relative  
 439 distance between the two ions changes during the course of the simulation, and at random periods  
 440 the two ions form an SSIP structure. In this simulation, we do not observe the formation of CIP  
 441 structure as it is not expected to occur at room temperature due to the very rigid hydrated structure  
 442 of magnesium and the limited MD timescales. Alternatively, we initialize the MD simulation with  
 443 CIP structure and run for 6 ns. The CIP structure remained stable during the simulation. Also, the  
 444 magnesium atom in the CIP structure has five water molecules, one water molecule less than the  
 445 SSIP structure in agreement with experiments and FF calculations(25,79). The CIP structure was  
 446 on average 0.09 eV lower than the SSIP structure, and 0.13 eV lower than the case where ions  
 447 were at least 3 water molecules apart from each other, confirming the relative stability of the CIP  
 448 structure compared to SSIP and SI in the solution. Our results are consistent with the experiment  
 449 that shows magnesium carbonate ion pair dissociates with 0.09 eV enthalpy difference(80).

450

451

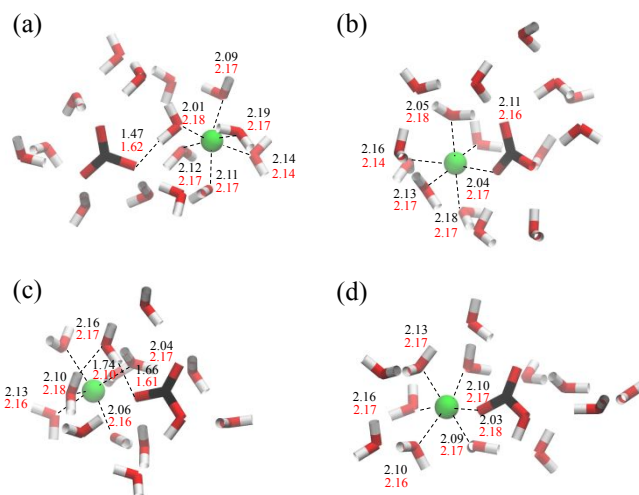


**Figure 5.** Magnesium-(bi)carbonate ion pairing clusters. a) Mg-CO<sub>3</sub> Solvent separated ion pair. b) Mg-CO<sub>3</sub> contact ion pair. c) [Mg-HCO<sub>3</sub>]<sup>+</sup> Solvent separated ion pair d) [Mg-HCO<sub>3</sub>]<sup>+</sup> contact ion pair. The distance values in black and red are derived from PBE-D3 and ReaxFF, respectively. Distances are in Angstroms.

#### 4- Applications of Aqueous and Interfacial FFs:

453 **4-1 H<sub>2</sub>CO<sub>3</sub> dissociation in water with Mg(OH)<sub>2</sub>:** Atmospheric carbon dioxide naturally dissolves  
 454 in water and partially reacts with it to produce carbonic acid and bicarbonate. The excess amount  
 455 of CO<sub>2</sub> from burning fossil fuels can negatively impact natural processes, one of which is the  
 456 acidification of the surface ocean. Carbonic acid dissociates to bicarbonate and proton, which  
 457 reacts with carbonates on the oceanic surfaces that can severely slow down the growth of coral  
 458 reefs(81). However, alkaline earth metals can neutralize carbonic acid by forming carbonate  
 459 minerals(82).

460 Here, we investigate the carbonic acid dissociation to bicarbonate and carbonate in the presence  
 461 of dissolved magnesium hydroxide Mg(OH)<sub>2</sub> in the water using our reactive FF. To this end, we  
 462 relax a neutral cell consisting of 250 water molecules, a carbonic acid molecule, and an Mg(OH)<sub>2</sub>  
 463 ion pair in NPT ensemble at room temperature and zero pressure using Nose-Hoover thermostat  
 464 and barostat with timestep of 0.25fs. After relaxation in NPT ensemble, we run the system in NVT  
 465 ensemble. We first observe that the hydroxide initially coordinated around magnesium readily  
 466 diffuses out into the solution through Grotthuss mechanism. Nevertheless, carbonic acid remained  
 467 intact in about 2 ns. Adding another Mg(OH)<sub>2</sub> monomer, resulted in a fast reaction between  
 468 carbonic acid with one of the hydroxide ions in less than 1ps to make bicarbonate as expected in  
 469 such a basic solution, as shown in **Fig. 6. a-c**. After about 100 ps, the other hydroxide structurally  
 470 diffuses toward the bicarbonate and grabs its proton and produces a carbonate ion, as shown in  
 471 **Fig. 6. a and Fig. 6 d-e**. Obviously because the hydroxide concentration is ~ 13 order of magnitude

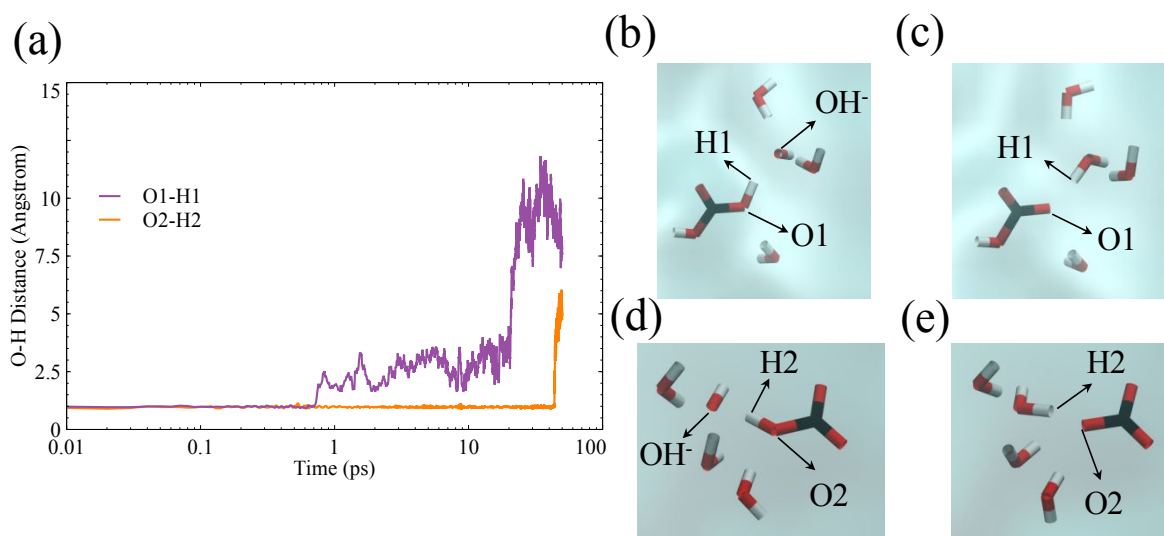


**Figure 6.** Carbonic acid dissociation in the presence of magnesium hydroxide. a) time-reaction for the deprotonation of carbonic acid. O1, H1, O2, and H2 are shown in the snapshots on the right. b) Carbonic acid in the solution before the reaction with the adjacent OH<sup>-</sup> occurs c) Bicarbonate is formed as the product of the deprotonation of carbonic acid through reaction with solvated hydroxide ion. d) Bicarbonate in the solution before the reaction with the adjacent OH<sup>-</sup> occurs e) carbonate is formed through the deprotonation of bicarbonate through reaction with a hydroxide. The cyan color in the background of snapshots represent the liquid water.

472 greater than its concentration at pH of 14, we cannot expect the carbonic acid dissociation to occur  
 473 this rapidly. However, our simulations show that the hydroxide, which diffuses structurally at a  
 474 high rate in bulk water can reach to carbonic acid to make a spontaneous proton transfer reaction.  
 475 With our reactive FF, we also observed the diffusion of surface hydroxide on metal divalent  
 476 containing minerals toward the carbonic acid at the thin water film. The limited space in the nano-  
 477 meter thin film in this system can substantially increase the rate of carbonic-acid-to-carbonate  
 478 reaction, although the diffusion of hydroxide in the structured water is hindered. This is the subject  
 479 of next section where we take brucite as a model surface to study this reaction.

480 We calculate the RDF for the three stages of the simulation described above. First, we fix the Ox-H  
 481 bonds of the carbonic acid and proceed with the simulation and output the trajectories. Then, we  
 482 unfix one of the Ox-H bonds and let the proton transfer happen to turn carbonic acid to bicarbonate,  
 483 and run the simulation again to produce outputs of the trajectories. Finally, we unfix the remaining  
 484 Ox-H bond of the bicarbonate until it turns into carbonate through another proton transfer reaction.  
 485 Again, we run the simulation and output the trajectories. For all the stages, we run the simulations  
 486 in NVT ensemble at room temperature using Nose-Hoover thermostat with timestep of 0.25 fs and  
 487 relaxation time of 25fs. We output the trajectories every 25fs over the course of 500 ps to produce  
 488 enough data for the radial distribution function (RDF) calculations. We also calculate the RDF for  
 489 Mg-Ow for the two solvated magnesium cations. The resulting RDFs are shown in **Fig. 7. a-d.**

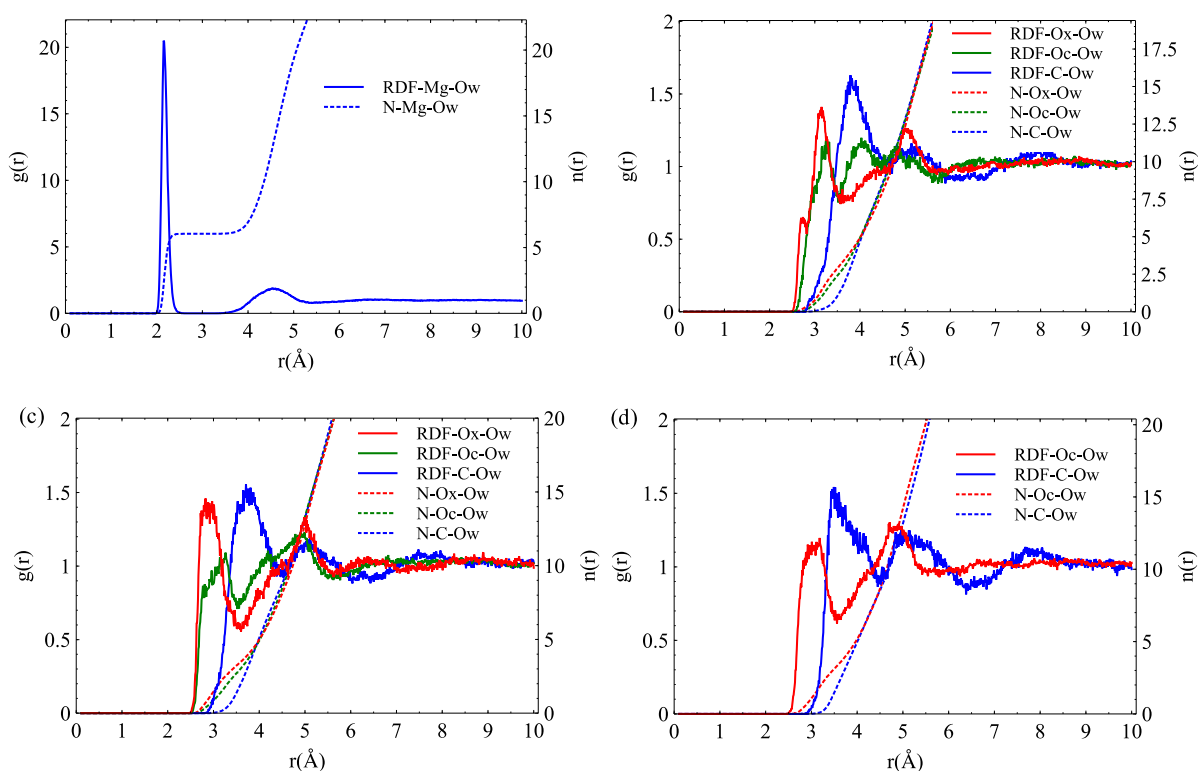


**Figure 7.**  $g(r)$  and coordination number,  $n(r)$ , for (a) Magnesium (b) Carbonic Acid (c) Bicarbonate and (d) Carbonate in the solution.  $g(r)$  is shown with solid line and  $n(r)$  is shown with dashed lines in all figures. Ow, Ox and Oc refer to water oxygen, hydroxyl oxygen, and carbonyl oxygen, respectively.

490 The RDF for Mg-Ow has one sharp peak at around 2.15 Å that corresponds to the first shell of  
491 water molecules that are tightly bound to the doubly charged magnesium cation as shown in **Fig.**  
492 **7. a**. The water coordination number for magnesium is derived to be 6, which is in agreement with  
493 experiment(83) and previous simulations(25,84). The carbonic acid contains two Ox and Oc which  
494 have different hydrogen bond networks as can be seen in the RDFs presented in **Fig. 7. b**. The first  
495 large peak for Ox-Ow is located at 3.13 Å which corresponds to the hydrogen bond that are  
496 accepted by the carbonic acid hydroxyl groups. A smaller peak for Ox-Ow is observed at 2.75 Å  
497 that is related to the hydrogen bonds donated by the hydroxyl of the carbonic acid. The first peak  
498 for Oc-Ow is located at 3.25 Å. By integrating the RDFs up to 3.75 Å for the first shell of water  
499 molecules around Ox, a hydration number of 3.8 is derived, see  $n(r)$  in **Fig. 7. b**. The hydration  
500 number of Oc is 3.4, which is slightly smaller than that of Ox, due to the stronger hydrogen bonds  
501 around hydroxyl groups that both donate and accept hydrogen bonds. Probing the hydration  
502 structure of carbonic acid through experiment is difficult, because of its short lifetime. However,  
503 quantum mechanics/molecular dynamics (QM/MM) simulations of aqueous carbonic acid shows  
504 a hydration number of 3.17 for Oc, which is close to our calculated value of 3.4(85).

505 For the bicarbonate simulation, the RDF for carbonyl oxygen (Oc) and hydroxyl oxygen (Ox) are  
506 shown in **Fig. 7. c**. The first peak for Ox-Ow is almost at 2.9 Å, while the first peak for Oc-Ow is  
507 slightly larger at around 3.1 Å, due to the stronger hydrogen bond of the hydroxyl oxygen. By  
508 integrating the RDF for the first peak up to 3.75 Å, the hydration number of Oc and Ox are derived  
509 to be 3.65 and 3.9, see the  $n(r)$  values in **Fig. 7. c**. These hydration numbers are both higher than  
510 their counterparts in carbonic acid. This is due to the charge of bicarbonate compared to the neutral  
511 carbonic acid as suggested by X-ray absorption spectroscopy measurements and Car-Parrinello  
512 MD simulations(85,86). However, our calculated hydration number for Oc is smaller than the  
513 derived value through QM/MM calculation which was 4.26(85). This could in part results from  
514 the charge equalization method in ReaxFF that gives a lower charge magnitude of bicarbonate in  
515 our simulations, which is around -0.85 that its formal charge of -1.

516 We also calculate the RDF and hydration numbers for carbonate as shown in **Fig. 7. d**. The first  
517 peak for the Oc-Ow is located at around 3.0 Å. Forcefield calculations done by Bruneval et al.(87)  
518 shows the peaks to be in a lower range at 2.69. The hydration number for Oc of the carbonate is  
519 4.08 if we integrate the RDF up to 3.75 Å. The forcefield calculation by Bruneval et al. shows a  
520 hydration number of 4.3, which like for the bicarbonate case could result from the lower charge  
521 magnitude of bicarbonate in our simulation ( $\sim -0.9$ ) that its formal charge of -2.

522 **4-2 Bicarbonate-Brucite interaction:** Ex-situ carbon mineralization can be achieved through the  
523 carbonation of mine wastes such as brucite [Mg(OH)<sub>2</sub>] in mafic and ultramafic mines(4,88). One  
524 study estimated that the accelerated carbonation of brucite in mine tailing could offset 22-57% of  
525 mine emissions(89). Previously, we showed through reactive molecular dynamics simulations that  
526 the presence of surface hydroxide initiates a long-range proton transfer to deprotonate bicarbonate  
527 in the interfacial water film on forsterite surfaces. Here, we examine the interaction of bicarbonate  
528 at the water-brucite interface.

529 We construct a simulation cell containing a brucite slab and a slit pore filled with liquid water. We  
530 fix the inner layers of the brucite so that they represent the bulk structure, and we let the first two  
531 layers move and interact with the water molecules on top. The size of the box is  
532  $18.5\text{\AA} \times 32.15\text{\AA} \times 57.10\text{\AA}$  in x, y and z direction, respectively. Then, we place a bicarbonate ion at  
533 the water-brucite interface and perform MD simulations in the NVT ensemble while fixing O-H  
534 bonds in water and bicarbonate to relax the system. Then, we remove the constraint on the bonds  
535 and let the system evolve naturally. Similar to the hydroxylated (010) forsterite surface simulated  
536 through reactive molecular dynamics(90), we observe spontaneous diffusion of surface OH-  
537 groups in the water layers adsorbed to the surface.

538 Such proton transfer reactions were also observed on other oxide surfaces in both simulations and  
539 experiments. Through *ab initio* MD simulations(91), it was shown that the rate of proton transfer  
540 reactions at the water-ZnO ( $10\bar{1}0$ ) surface substantially increases when the number of water layers  
541 increases from one layer to a liquid multi-layer. Also, *ab initio*-based deep neural network analysis  
542 was able to show long-range proton transfer through water molecules at the water-TiO<sub>2</sub>  
543 interface(92). Moreover, scanning tunneling microscopy experiments on FeO(93) and TiO<sub>2</sub>(94)  
544 monolayers and single-molecule localization microscopy on defective boron nitride layers(95)  
545 unveil the proton transport at the solid-water interface. Recently, spectral single-molecule scanning  
546 tunneling microscopy and *ab initio* simulations(96) demonstrated higher proton diffusivity along  
547 the surface of boron nitride when it is in contact with a binary water-methanol solution rather than  
548 water- only solution.

549 After few picoseconds in our simulation on the brucite surface, we observe that a hydrogen-bond  
550 network forms between the bicarbonate and a surface hydroxide leading to a chain of proton  
551 transfer reactions that deprotonates the bicarbonate at the end, as shown in **Fig.8. a-d**. The  
552 hydroxide ion structurally diffuses from the surface toward the bicarbonate in the interfacial water  
553 film. Structural diffusion, often called “Grotthuss diffusion,” is the hopping of a proton from a  
554 hydronium ion to a neighboring water molecule or from a water molecule to a neighboring  
555 hydroxide. It involves breakage and formation of O-H bonds as the proton migrates between water  
556 molecules. It is much faster than vehicular diffusion. The centers of charge and mass move  
557 together.(97) Similarly, hydroxide groups can structurally diffuse through water molecules as  
558 observed in biological systems and enzymatic reactions(98,99).

559 We also calculate the RDF for surface magnesium, carbonic acid, bicarbonate, and carbonate for  
560 the simulation on the surface of brucite. Initially, we fix the carbonic acid in the water layers  $5\text{\AA}$   
561 away from the surface of brucite. To avoid spontaneous proton transfer that transforms the  
562 carbonic acid to bicarbonate and then to carbonate, we fix the O-H bonds of the hydroxyl group in  
563 carbonic acid. We run the simulation in NVT ensemble for 250ps, and output the trajectories every  
564 25fs to produce data for RDF calculation. Other simulation settings are similar to those we used  
565 for carbonic acid deprotonation described in section 4-1.

566 The RDF for surface magnesium (Ms) and oxygen of water and surface hydroxide (O\*) is shown  
567 in **Figure 8. e**. The first peak is located at  $2.13\text{\AA}$ , and a coordination number of 2.7 is derived for  
568 the first shell of O\*, where two surface hydroxides are always present. The RDFs calculated for



569 carbonic acid on the surface are shown in **Figure 8. f**. Like carbonic acid in the solution, the RDF  
 570 for Ox-O\* has two peaks close to each other, one at 2.6Å that corresponds to the accepted hydrogen  
 571 bond and another at 3.12 that corresponds to the donated hydrogen bond. Interestingly, the  
 572 hydration number for Ox is about 5.3 which is significantly larger than its counterpart in the  
 573 solution which is 3.8. This can be the result of denser water layers with stronger hydrogen bonds  
 574 compared to liquid water. This could also be the reason for the RDF for Oc-O\* to have its first two  
 575 peaks closer to each other than what we observe in the solution.

576 For the case of bicarbonate in the water layers on top of brucite, we see that the first peaks for both  
 577 RDFs of Ox-O\* and Oc-O\* shift toward smaller distances as shown in **Figure 8. g**. We attribute

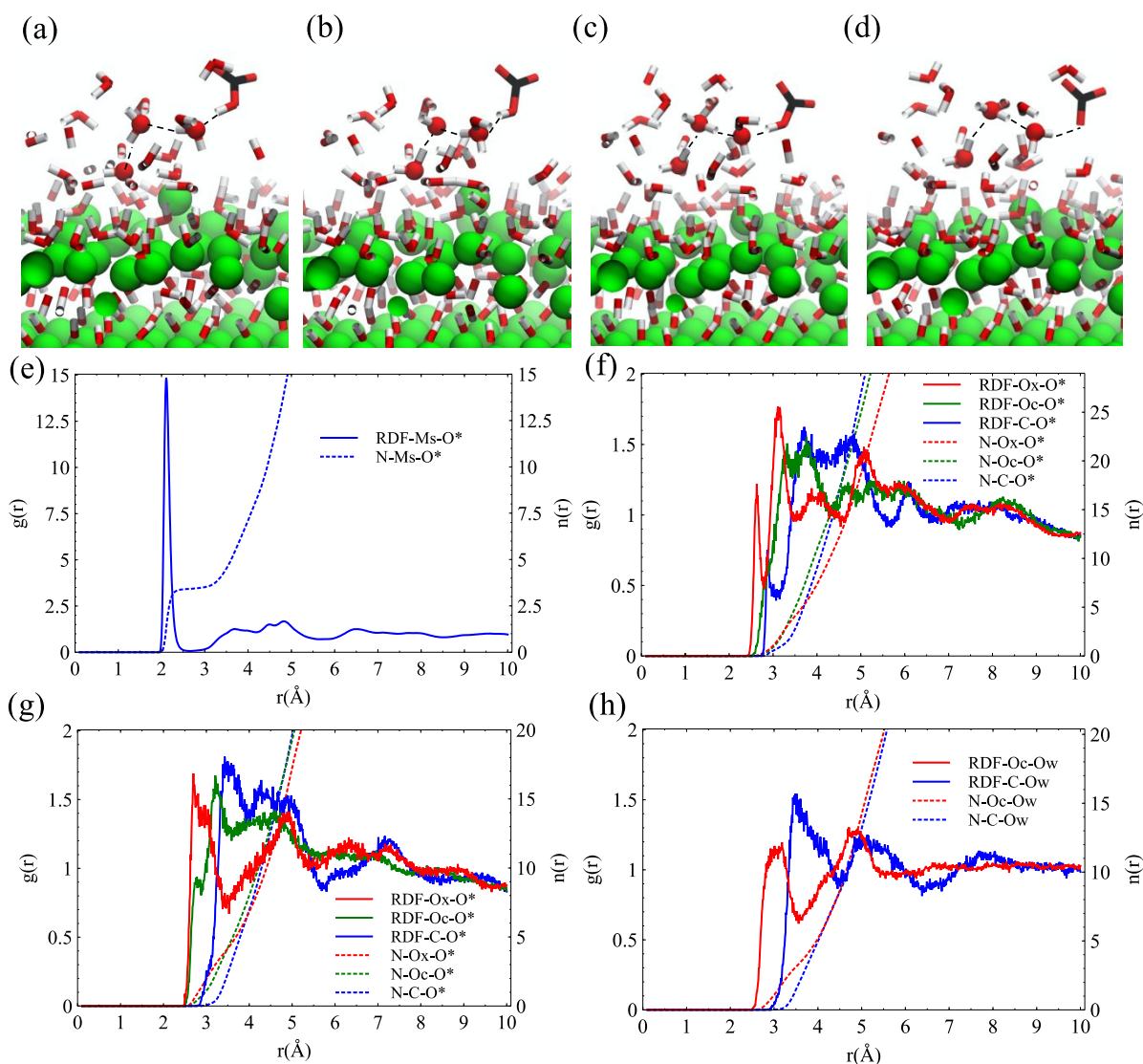


**Figure 8.** The deprotonation of bicarbonate at the brucite-water interface. From (a) to (c) the hydroxide in the first water layer diffuses toward the bicarbonate. (d) The bicarbonate deprotonates to carbonate hydrating a neighboring hydroxyl group. (e)  $g(r)$  and coordination number,  $n(r)$ , for magnesium-water on the surface of brucite. (f)  $g(r)$  and  $n(r)$  for carbonic acid on the surface of brucite. (g)  $g(r)$  and  $n(r)$  for bicarbonate on the surface of brucite. (h)  $g(r)$  and  $n(r)$  for carbonate on the surface of brucite.  $g(r)$  is shown with solid line and  $n(r)$  is shown with dashed lines in all figures. O\*, Ox and Oc refer to water/surface hydroxide oxygen, hydroxyl oxygen, and carbonyl oxygen respectively. Ms represents surface magnesium.

578 this systematic shift is the result of different water permittivity in the water layers than that of  
 579 liquid water. Therefore, compared to liquid water, the negative charge of bicarbonate results in  
 580 stronger electrostatics field that strengthens hydrogen bonds with dipolar water molecules. As  
 581 shown in in **Figure 8. h**, we could not observe any further shift for the doubly-charged carbonate,  
 582 that is related to the smaller charge magnitude of carbonate ( $\sim 1.05$ ) than its formal charge of 2.

583 The ReaxFF simulations also provide a detailed picture of the dynamics of structural hydroxide  
 584 diffusion on the brucite surface. Since the adsorbed water layers on the brucite surface are more  
 585 structured than liquid water, and also because the positively-charged magnesium cations attract  
 586 hydroxide ions, we expect a hindered interfacial diffusion for hydroxide ions. To show this  
 587 quantitatively, we run further simulations to calculate the diffusion constant of hydroxide ions  
 588 adsorbed on the surface of brucite. To this end, we calculate the diffusion constant of  $\text{OH}^-$  in XY  
 589 direction, parallel to the brucite surface, and in the Z direction s perpendicular to the surface using  
 590 the Einstein relation:

$$591 \quad D_{xy} = \frac{1}{4t} \langle |r_{xy}(t) - r_{xy}|^2 \rangle \quad (11)$$

$$592 \quad D_z = \frac{1}{t} \langle |r_z(t) - r_z|^2 \rangle \quad (12)$$

593 In which  $r$  represents the position of the particle, and  $t$  is the time.  $\langle |r_{xy}(t) - r_{xy}|^2 \rangle$  and  
 594  $\langle |r_z(t) - r_z|^2 \rangle$  are the mean-square displacement (MSD) in the XY plane and in the Z direction,  
 595 respectively.

596 To calculate the MSD for hydroxide ions on the surface, we randomly pick seven hydroxides and  
 597 track the trajectory of the  $\text{O}^*$  of the  $\text{OH}^-$ . (100) The index  $\text{O}^*$  can change during the course of the  
 598 simulation as proton transfer can happen between water molecules and the  $\text{OH}^-$ . We construct a  
 599 similar system as in section 4-2, containing brucite slab in contact with water while letting the first  
 600 two layers of brucite move and fix the inner layers. We initially relax the system in the NVT  
 601 ensemble at room temperature for 200 ps using timesteps of 0.25 fs and a Nose-Hoover thermostat  
 602 with relaxation time of 25 fs. After the system is relaxed, we change the ensemble to NVE to avoid  
 603 thermostat effects that can interfere with the trajectory of atoms. We run the system for 125 ps,

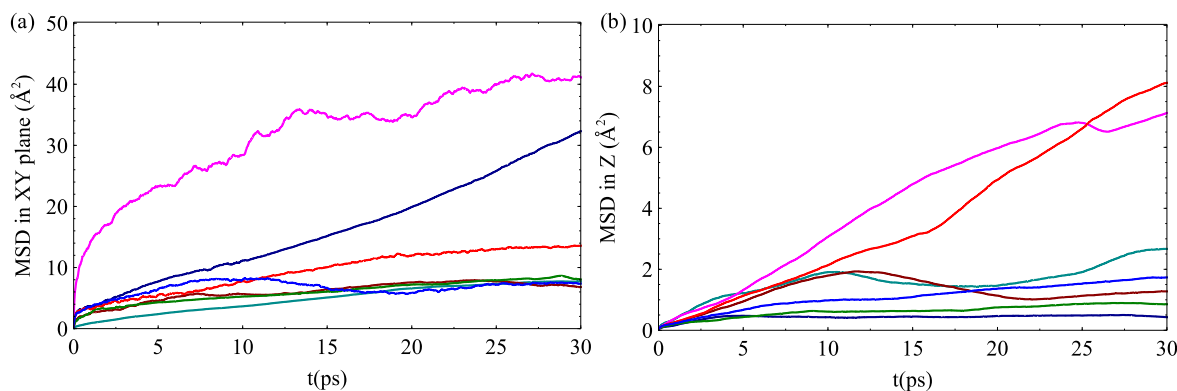


**Figure 9.** Mean-square displacement (MSD) for hydroxide ions on the surface of brucite. (a) MSD in the XY plane parallel to the surface. (b) MSD in the Z direction perpendicular to the surface. Different colors represent the displacement of seven randomly picked hydroxide ions on the surface of brucite.



604 and output trajectories every 2.5 fs to be used for the calculation of MSD. The resulting MSD up  
605 to 30 ps for the seven randomly picked hydroxide ions are shown in **Fig. 9. a-b**.

606 We note that the slope of the MSDs are not quite linear compared to the MSDs of hydroxide ions  
607 in liquid water resulted from the same forcefield(100). This is due to the presence of magnesium  
608 cations on the surface of brucite that can trap the hydroxide ions. Here, we use the linear part of  
609 the MSDs with maximum slope for the calculation of diffusion constants. We calculate the  
610 diffusion constant for each  $O^*$  from the linear parts of the resulted MSDs. For the diffusion in XY  
611 plane,  $D_{xy}$  ranges between 0.04 and 0.18  $\text{\AA}^2/\text{ps}$ , while  $D_z$  ranges between 0.16 and 0.76  $\text{\AA}^2/\text{ps}$ .  
612 Based on the similar ReaxFF forcefield for water, the reported diffusion constant for the hydroxide  
613 ion in water is 1.03  $\text{\AA}^2/\text{ps}$  which is higher than our calculated diffusion constants. This difference  
614 can arise from the more structured water layers on the hydrophilic surface of brucite. The  
615 difference between  $D_{xy}$  and  $D_z$  and the variable diffusion constant derived for each of the randomly  
616 selected hydroxide ions show anisotropy and heterogeneity in the interfacial diffusion process of  
617 these species in the adsorbed water layers. It is noteworthy that a second-generation ReaxFF water  
618 model can better predict the diffusion of hydroxide and hydronium ions compared to the one we  
619 used in our paper(100). However, because the first generation ReaxFF water model is fitted and  
620 tested for the proton transfer between water and carbonic acid, which is essential for modelling  
621 magnesium carbonate systems, we use the first generation ReaxFF water model. Nevertheless, we  
622 carefully analyzed the proton transfer between bicarbonate and forsterite surface using both first-  
623 and second-generation ReaxFF water model. We find that the free energy barrier for the long-  
624 range proton transfer that transforms bicarbonate to carbonate is not significantly affected by the  
625 water model.

626 **4-3 Free energy calculation of  $\text{Mg-CO}_3$  surface complex formation on the surface of**  
627 **forsterite:** The knowledge of the thermodynamics of ion-pairing at the solid-liquid interface is  
628 critical for understanding heterogeneous nucleation and growth. However, ion-pairing in the  
629 solution and at the solid-liquid interface is experimentally challenging to probe due to the small  
630 size of the ions and their short lifetime. On the other hand, quantum mechanical calculations are  
631 also problematic due to their high computational cost and the uncertainty about van der Waals  
632 interactions in the liquid phase. Nonetheless, molecular simulations can provide insight into the  
633 kinetics of ion interactions if accurate FFs are available. A thermodynamically stable FF was  
634 successfully able to calculate the free energy barrier for the pairing of ( $\text{Ca}^{2+}$ ,  $\text{Mg}^{2+}$ ,  $\text{Sr}^{2+}$ ) cations  
635 and bicarbonate and carbonate species in the solution. However, metal cations on the surface of  
636 metal-silicates and metal-oxides are sometimes coordinated with hydroxide ions. Therefore,  
637 surface complex formation with ions like carbonate and bicarbonate may require a proton transfer  
638 reaction from the first shell of metal cations to their second shell, especially for magnesium cations  
639 tightly bound to their water/hydroxide shell. This calls for a reactive FF like ReaxFF, which can  
640 model the structural diffusion of proton/hydroxide.

641 Here, we do the free energy calculation for the carbonate adsorption on the (010) hydroxylated  
642 surface of forsterite. First, we construct a slab of forsterite with 9 layers and an interlayer space  
643 with a size of 27  $\text{\AA}$ . We fill the interlayer space with water such that the density at the middle 10  
644  $\text{\AA}$  is 0.91  $\text{g}/\text{cm}^3$  consistent with the density of liquid water when relaxed with ReaxFF. We fix the  
645 forsterite slab except for the first two surface layers at the top and the bottom. The energetics of  
646 the adsorption of carbonate on the forsterite surface is determined via the umbrella sampling (US)

647 technique as implemented in the “PLUMED 2.5” add-on package to LAMMPS(101). Here, we  
 648 use a biased harmonic spring with a stiffness of  $140 \text{ kcal/mol}\text{\AA}^{-2}$  between the center of mass of the  
 649 carbonate and a fixed reference  $\text{Me}^{2+}$  atom in the inner layer of forsterite respectively. The normal  
 650 distance to the solid surface is taken as the “collective variable” and sampling windows are  
 651 separated by  $0.1 \text{ \AA}$ . Histograms of the distribution of the collective variables were produced after  
 652 100 ps of equilibration phase, and another 250ps of the production phase of MD runs at 300 K in  
 653 the NVT ensemble. The substrate (except the first two layers) were fixed. A weak harmonic  
 654 potential was also considered in the ‘xy’ plane (parallel to the surface) to keep the carbonate in the  
 655 desired adsorption site, enclosed in a cylinder. The free energy difference is then obtained via the  
 656 weighted histogram analysis method (WHAM)(102).

657 Our PMF calculations show that the formation of  $\text{Mg} \equiv \text{CO}_3$  surface complex on a random Mg  
 658 site is relatively stable. This surface complex formation is made possible through a proton transfer  
 659 step in which the  $\text{OH}^-$  attached to the surface grabs a proton from the second water shell. Another  
 660 water molecule leaves the first shell to make room for the carbonate (see **Fig. 10. a-c**). The energy  
 661 barrier for this Mg- $\text{CO}_3$  surface complex formation is  $0.21 \text{ eV}$ , about  $0.04 \text{ eV}$  lower than the free  
 662 energy required for their pairing in bulk water(25). This has major implications on the nucleation  
 663 stage. It reduces the magnesium dissolution energy barrier and can enhance the growth of  
 664 magnesite crystal since ion pairs could readily attach to the crystal. This can also explain the  
 665 anomalous low activation energy barrier for the nucleation and growth of magnesite at low  
 666 temperature(17) when reactions occur at the thin water film formed on forsterite.

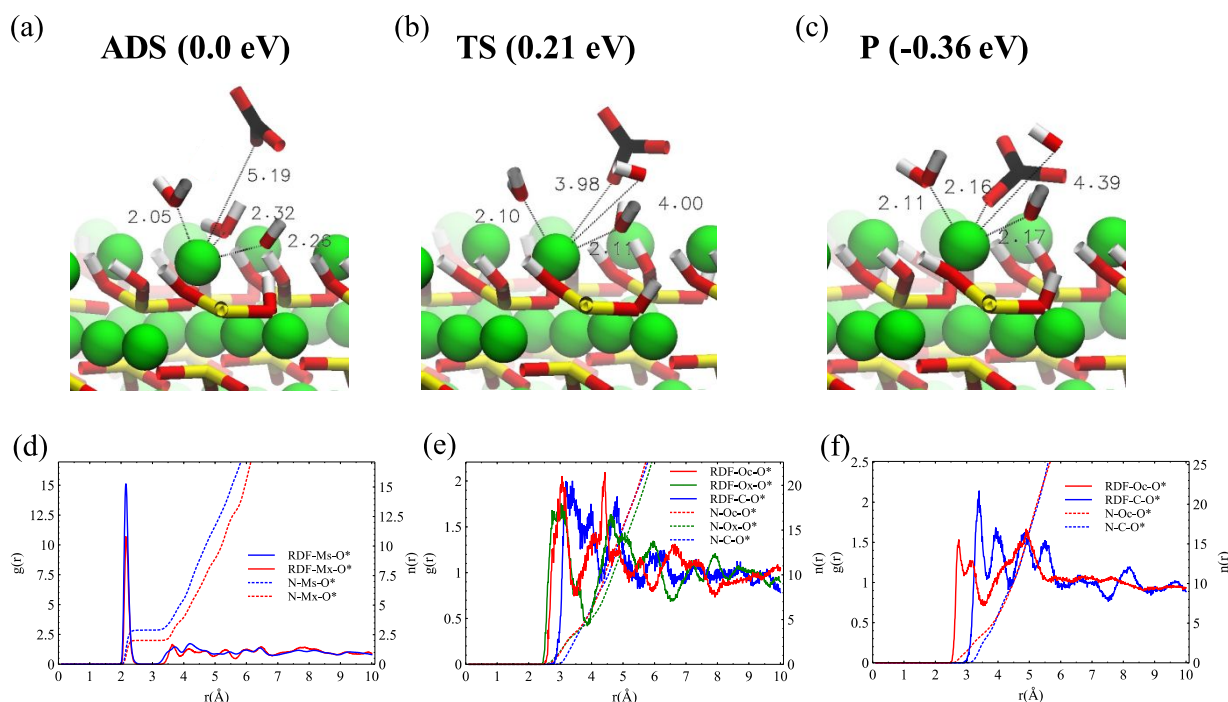


**Figure 10.** Adsorption of  $\text{CO}_3^{2-}$  on hydroxylated  $\{010\}$  surface of Forsterite. (a-c) (ADS) adsorbate state of  $\text{CO}_3^{2-}$  as determined by PMF calculations. Two water molecules as well as one hydroxide are coordinated around surface Magnesium. (TS) transition state. (P) product state. (d)  $g(r)$  and coordination number,  $n(r)$ , for (d) Magnesium (e) Bicarbonate and (f) Carbonate on the surface forsterite.  $g(r)$  is shown with solid line and  $n(r)$  is shown with dashed lines in all figures.

667 We calculate the RDF for surface magnesium and carbonate at two windows that we used for the  
668 free energy calculation: 1) When the carbonate is 5Å away from the surface. 3) When the carbonate  
669 is adsorbed on the surface and is paired with two surface magnesium atoms. The first peak of RDF  
670 for the surface magnesium (Ms) and water is located at 2.15Å similar to the location of the water  
671 in the first hydration shell of magnesium solvated in water as shown in **Fig. 10. d**. The water  
672 coordination number for Ms is 2.85. We label the surface magnesium that is coordinated with  
673 carbonate as Mx as shown in **Fig. 10. d**. Although, the location of the first peak for Mx-O\* is the  
674 same as Ms-O\*, the water coordination number for Mx is dropped to 2. As stated in the previous  
675 paragraph, we observe that for the magnesium-carbonate surface complex formation, the  
676 coordinated hydroxide grabs a proton from a nearby water molecule, and one water molecule is  
677 removed from the first coordination shell of Mx. When the carbonate is adsorbed on the surface,  
678 we need to differentiate two carbonate oxygens that are paired to surface magnesiums (Ox) with  
679 the one that is oriented toward the solution (Oc). As shown in **Fig. 10. e**, the hydration number for  
680 Oc is ~4.3, which is higher than the hydration number for oxygens of the carbonate in the solution,  
681 due to the higher density of layered water on top of forsterite. When the carbonate is distanced 5Å  
682 from the surface, we observe two peaks in the RDF for Oc-O\* as shown in **Fig. 10. f**. By visual  
683 inspection, we find that the carbonate is not able to rotate freely as in the solution, due to the  
684 electrostatic field it senses from the surface magnesium. Rather, one carbonate oxygen remains  
685 oriented toward to the surface for the entire time of the simulation. The hydration number of the  
686 carbonate oxygen (Oc) is 4.3, higher than its solution counterpart.

### 687 **3- Conclusion:**

688 We develop two reactive FFs for modeling aqueous magnesium carbonate and Mg/O/Si/C/H  
689 containing solids and their interfaces with water. We successfully parameterize the FFs to the  
690 configurations and mechanical properties of magnesite, magnesium hydroxide, magnesium oxide,  
691 and other relevant crystals. Additionally, the structures and hydration energies of magnesium are  
692 included in the list of observables for the aqueous FF. After deriving the FF parameters, we test  
693 the transferability of the interfacial FF to other prevalent magnesium-containing minerals in the  
694 context of carbon sequestration, including the bulk structure of forsterite, nesquehonite, dolomite,  
695 and diopside. Not only the lattice properties of these crystals are captured well with our FF, but  
696 also the bulk modulus of dolomite and some of its elastic constants are predicted accurately.

697 Next, the interfacial structure of magnesium (-carbonate, -silicate, and -oxide) minerals when dry  
698 or in contact with a single water molecule are investigated using both DFT calculations and  
699 interfacial ReaxFF. Although the geometry of all dry surfaces is similar in both methods, the  
700 hydration energies are overestimated when calculated through the reactive FF. Some hydrogen  
701 bonds are underestimated, except for the case of “side water” adsorption on the surface of  
702 forsterite. The discrepancy of hydration energies and hydrogen bond distances stems partly from  
703 the oxygen-hydrogen interaction parameters in ReaxFF that are mainly fitted to describe liquid  
704 water, and partly from the absence of Mg-O-O and Mg-O-H parameters in our forcefield. Unlike  
705 the single water molecule adsorption, the adsorption energies resulted from ReaxFF for two to five

706 water monolayers are in agreement with the experiment. This makes our FF suitable to study  
707 reactions at the water-forsterite interface when few water monolayers are present.

708 Then, we study the interaction of magnesium and (bi)carbonate in gaseous clusters and liquid  
709 water. Our calculations for magnesium-(bi)carbonate ion-pairing through the fitted aqueous FF  
710 agree well with DFT results. Although the obtained energies for SSIP structures are lower than the  
711 CIP structure in gaseous clusters, the averaged potential energies in liquid water confirm the  
712 relative stability of CIP to SSIP and SSIP to SI structures. This enables our force field to study  
713 homogeneous nucleation of magnesite, hydromagnesite, nesquehonite, and amorphous  
714 magnesium carbonate phases. We also check the applicability of the derived reactive forcefields  
715 for the dissociation of carbonic acid in liquid water that contains magnesium and hydroxide ions  
716 and the interfacial water layers on top of the brucite surface. Our simulations demonstrate the  
717 migration of hydroxide ions that leads to carbonate production, whether in liquid water or at the  
718 interface of brucite. Proton transfer reactions at the interface of metal oxides have been previously  
719 observed through both experiments and quantum mechanical calculations.

720 The observed proton transfer at the hydroxylated-solid-water interface has significant implications  
721 on the nucleation of magnesium carbonate phases at geological conditions. It can explain the  
722 anomalously low activation energy barrier for the formation of magnesite. At the molecular scale,  
723 it can manifest both through the pairing of the dissolved surface magnesium and carbonate at the  
724 thin water film or the formation of neutral magnesium-carbonate surface complexes that can  
725 dissolve faster than the magnesium cation(12). Here, we show that a stable Mg-CO<sub>3</sub> surface  
726 complex can form on the hydroxylated surface of forsterite with a low energy barrier. However,  
727 more elaborate free energy calculations that consist of magnesium-water coordination number as  
728 a collective variable are needed for more accurate energy barrier calculations.

#### 729 **Acknowledgements:**

730 This work was primarily supported by Early Career Award Program from the DOE Office of  
731 Science, Basic Energy Sciences, Division of Chemical, Biological and Geological Sciences under  
732 contract no. DE-SC0022301. The brucite calculations are supported by the National Science  
733 Foundation under Awards No. CMMI-2103125. Any Opinions, findings and conclusions or  
734 recommendations expressed in this material are those of the authors and do not necessarily reflect  
735 those of the funding agencies. MJAQ also gratefully acknowledges financial support through  
736 Hellman Fellowship. We thank Drs. Andreas Funk and Quin Miller for fruitful discussions.

#### 737 **Competing interests:**

738 The authors declare no competing interests.

#### 739 **Data Availability:**

740 The modified LAMMPS source code for constant cation charge ReaxFF simulations are available  
741 upon request from the corresponding author.

742

743 **References:**

- 744 1. Silva JJRF da, Williams RJP. *The Biological Chemistry of the Elements: The Inorganic Chemistry of Life*.  
745 OUP Oxford; 2001. 606 p.
- 746 2. Taub AI, Luo AA. *Advanced lightweight materials and manufacturing processes for automotive applications*.  
747 *MRS Bull.* 2015 Dec;40(12):1045–54.
- 748 3. Höche D, Lamaka SV, Vaghefinazari B, Braun T, Petrauskas RP, Fichtner M, et al. Performance boost for  
749 primary magnesium cells using iron complexing agents as electrolyte additives. *Sci Rep.* 2018 May  
750 15;8(1):7578.
- 751 4. Snæbjörnsdóttir SÓ, Sigfússon B, Marieni C, Goldberg D, Gislaon SR, Oelkers EH. Carbon dioxide storage  
752 through mineral carbonation. *Nat Rev Earth Environ.* 2020 Feb;1(2):90–102.
- 753 5. Pavlov M, Siegbahn PEM, Sandström M. Hydration of Beryllium, Magnesium, Calcium, and Zinc Ions Using  
754 Density Functional Theory. *J Phys Chem A.* 1998 Jan 1;102(1):219–28.
- 755 6. Markham GD, Glusker JP, Bock CW. The Arrangement of First- and Second-Sphere Water Molecules in  
756 Divalent Magnesium Complexes: Results from Molecular Orbital and Density Functional Theory and from  
757 Structural Crystallography. *J Phys Chem B.* 2002 May 1;106(19):5118–34.
- 758 7. Xu J, Yan C, Zhang F, Konishi H, Xu H, Teng HH. Testing the cation-hydration effect on the crystallization  
759 of Ca–Mg–CO<sub>3</sub> systems. *Proc Natl Acad Sci.* 2013 Oct 29;110(44):17750–5.
- 760 8. Qafoku O, Dixon DA, Rosso KM, Schaef HT, Bowden ME, Arey BW, et al. Dynamics of Magnesite  
761 Formation at Low Temperature and High pCO<sub>2</sub> in Aqueous Solution. *Environ Sci Technol.* 2015 Sep  
762 1;49(17):10736–44.
- 763 9. Qafoku O, Hu J, Hess NJ, Hu MY, Ilton ES, Feng J, et al. Formation of submicron magnesite during reaction  
764 of natural forsterite in H<sub>2</sub>O-saturated supercritical CO<sub>2</sub>. *Geochim Cosmochim Acta.* 2014 Jun 1;134:197–  
765 209.
- 766 10. Felmy AR, Qafoku O, Arey BW, Hu JZ, Hu M, Todd Schaef H, et al. Reaction of water-saturated supercritical  
767 CO<sub>2</sub> with forsterite: Evidence for magnesite formation at low temperatures. *Geochim Cosmochim Acta.* 2012  
768 Aug 15;91:271–82.
- 769 11. Miller QRS, Ilton ES, Qafoku O, Dixon DA, Vasiliu M, Thompson CJ, et al. Water Structure Controls  
770 Carbonic Acid Formation in Adsorbed Water Films. *J Phys Chem Lett.* 2018 Sep 6;9(17):4988–94.
- 771 12. Miller QRS, Dixon DA, Burton SD, Walter ED, Hoyt DW, McNeill AS, et al. Surface-Catalyzed Oxygen  
772 Exchange during Mineral Carbonation in Nanoscale Water Films. *J Phys Chem C.* 2019 May  
773 23;123(20):12871–85.
- 774 13. Loring JS, Chen J, Bénézeth P, Qafoku O, Ilton ES, Washton NM, et al. Evidence for Carbonate Surface  
775 Complexation during Forsterite Carbonation in Wet Supercritical Carbon Dioxide. *Langmuir.* 2015 Jul  
776 14;31(27):7533–43.
- 777 14. Miller QRS, Schaef HT, Kaszuba JP, Gadikota G, McGrail BP, Rosso KM. Quantitative Review of Olivine  
778 Carbonation Kinetics: Reactivity Trends, Mechanistic Insights, and Research Frontiers. *Environ Sci Technol*  
779 *Lett.* 2019 Aug 13;6(8):431–42.
- 780 15. Placencia-Gómez E, Kerisit SN, Mehta HS, Qafoku O, Thompson CJ, Graham TR, et al. Critical Water  
781 Coverage during Forsterite Carbonation in Thin Water Films: Activating Dissolution and Mass Transport.  
782 *Environ Sci Technol.* 2020 Jun 2;54(11):6888–99.

- 783 16. S. Miller QR, P. Kaszuba J, N. Kerisit S, Todd Schaef H, E. Bowden M, Peter McGrail B, et al. Emerging  
784 investigator series: ion diffusivities in nanoconfined interfacial water films contribute to mineral carbonation  
785 thresholds. *Environ Sci Nano*. 2020;7(4):1068–81.
- 786 17. S. Miller QR, P. Kaszuba J, T. Schaef H, E. Bowden M, Peter McGrail B, M. Rosso K. Anomalously low  
787 activation energy of nanoconfined MgCO<sub>3</sub> precipitation. *Chem Commun*. 2019;55(48):6835–7.
- 788 18. Liu T, Gautam S, Wang H-W, M. Anovitz L, Mamontov E, F. Allard L, et al. Structure and dynamics of water  
789 on the forsterite surface. *Phys Chem Chem Phys*. 2018;20(44):27822–9.
- 790 19. Zachara J, Brantley S, Chorover J, Ewing R, Kerisit S, Liu C, et al. Internal Domains of Natural Porous Media  
791 Revealed: Critical Locations for Transport, Storage, and Chemical Reaction. *Environ Sci Technol*. 2016 Mar  
792 15;50(6):2811–29.
- 793 20. Gautier Q, Bénézech P, Schott J. Magnesite growth inhibition by organic ligands: An experimental study at  
794 100, 120 and 146°C. *Geochim Cosmochim Acta*. 2016 May 15;181:101–25.
- 795 21. Miller QRS, Kaszuba JP, Schaef HT, Bowden ME, McGrail BP. Impacts of Organic Ligands on Forsterite  
796 Reactivity in Supercritical CO<sub>2</sub> Fluids. *Environ Sci Technol*. 2015 Apr 7;49(7):4724–34.
- 797 22. Morrow CP, Olsen AA, Kubicki JD. Quantum mechanical modeling of hydrolysis and H<sub>2</sub>O-exchange in Mg-,  
798 Ca-, and Ni-silicate clusters: Implications for dissolution mechanisms of olivine minerals. *Am Mineral*. 2014  
799 Nov 1;99(11–12):2303–12.
- 800 23. Prigobbe V, Suarez Negreira A, Wilcox J. Interaction between Olivine and Water Based on Density  
801 Functional Theory Calculations. *J Phys Chem C*. 2013 Oct 17;117(41):21203–16.
- 802 24. Kerisit S, Weare JH, Felmy AR. Structure and dynamics of forsterite–scCO<sub>2</sub>/H<sub>2</sub>O interfaces as a function of  
803 water content. *Geochim Cosmochim Acta*. 2012 May 1;84:137–51.
- 804 25. Raiteri P, Demichelis R, Gale JD. Thermodynamically Consistent Force Field for Molecular Dynamics  
805 Simulations of Alkaline-Earth Carbonates and Their Aqueous Speciation. *J Phys Chem C*. 2015 Oct  
806 29;119(43):24447–58.
- 807 26. D. Gale J, Raiteri P, Duin ACT van. A reactive force field for aqueous-calcium carbonate systems. *Phys Chem  
808 Chem Phys*. 2011;13(37):16666–79.
- 809 27. Russo MF, van Duin ACT. Atomistic-scale simulations of chemical reactions: Bridging from quantum  
810 chemistry to engineering. *Nucl Instrum Methods Phys Res Sect B Beam Interact Mater At*. 2011 Jul  
811 15;269(14):1549–54.
- 812 28. Song GL, Atrens A. Corrosion Mechanisms of Magnesium Alloys. *Adv Eng Mater*. 1999;1(1):11–33.
- 813 29. Rappe AK, Goddard WA. Charge equilibration for molecular dynamics simulations. *J Phys Chem*. 1991 Apr  
814 1;95(8):3358–63.
- 815 30. Nakano A. Parallel multilevel preconditioned conjugate-gradient approach to variable-charge molecular  
816 dynamics. *Comput Phys Commun*. 1997 Aug 1;104(1):59–69.
- 817 31. Aktulga HM, Fogarty JC, Pandit SA, Grama AY. Parallel reactive molecular dynamics: Numerical methods  
818 and algorithmic techniques. *Parallel Comput*. 2012 Apr 1;38(4):245–59.
- 819 32. Mortier W, Ghosh SK, Shankar S. Electronegativity Equalization Methods for the Calculation of Atomic  
820 Charges in Molecules. *J Am Chem Soc*. 1986 Jan;108(15):4315–20.

- 821 33. Vajeeston P, Ravindran P, Kjekshus A, Fjellvåg H. Pressure-Induced Structural Transitions in  
822  $\text{MgH}_2$ . Phys Rev Lett. 2002 Oct 8;89(17):175506.
- 823 34. Karen P, Kjekshus A, Huang Q, Karen VL. The crystal structure of magnesium dicarbide. J Alloys Compd.  
824 1999 Jan 15;282(1):72–5.
- 825 35. Xia X, Weidner DJ, Zhao H. Equation of state of brucite; single-crystal Brillouin spectroscopy study and  
826 polycrystalline pressure-volume-temperature measurement. Am Mineral. 1998 Feb 1;83(1–2):68–74.
- 827 36. Zigan F, Rothbauer R. Neutronenbeugungsmessungen am brucit. Neues Jahrb Mineral Monatshefte.  
828 1967;1967:137–43.
- 829 37. Sasaki S, Fujino K, Takéuchi Y. X-Ray Determination of Electron-Density Distributions in Oxides, MgO,  
830 MnO, CoO, and NiO, and Atomic Scattering Factors of their Constituent Atoms. Proc Jpn Acad Ser B.  
831 1979;55(2):43–8.
- 832 38. Ross NL. The equation of state and high-pressure behavior of magnesite. Am Mineral. 2015;82(7–8):682–8.
- 833 39. Catti M, Pavese A, Dovesi R, Saunders VR. Static lattice and electron properties of  
834  $\text{MgCO}_3$  (magnesite) calculated by ab initio periodic Hartree-Fock methods. Phys Rev B.  
835 1993 Apr 15;47(15):9189–98.
- 836 40. Markham GD, Glusker JP, Bock CL, Trachtman M, Bock CW. Hydration Energies of Divalent Beryllium and  
837 Magnesium Ions: An ab Initio Molecular Orbital Study. J Phys Chem. 1996 Jan 1;100(9):3488–97.
- 838 41. Frisch MJ, Trucks GW, Schlegel HB, Scuseria GE, Robb MA, Cheeseman JR, et al. Gaussian 16. Revis A.  
839 2016;3.
- 840 42. Becke AD. Density-functional thermochemistry. III. The role of exact exchange. J Chem Phys. 1993 Apr  
841 1;98(7):5648–52.
- 842 43. Lee C, Yang W, Parr RG. Development of the Colle-Salvetti correlation-energy formula into a functional of  
843 the electron density. Phys Rev B. 1988 Jan 15;37(2):785–9.
- 844 44. Li X, Frisch MJ. Energy-Represented Direct Inversion in the Iterative Subspace within a Hybrid Geometry  
845 Optimization Method. J Chem Theory Comput. 2006 May;2(3):835–9.
- 846 45. Krack M, Köster AM. An adaptive numerical integrator for molecular integrals. J Chem Phys. 1998 Feb  
847 22;108(8):3226–34.
- 848 46. Grimme S, Antony J, Ehrlich S, Krieg H. A consistent and accurate ab initio parametrization of density  
849 functional dispersion correction (DFT-D) for the 94 elements H-Pu. J Chem Phys. 2010 Apr 1;132:154104–  
850 154104.
- 851 47. Grimme S, Ehrlich S, Goerigk L. Effect of the damping function in dispersion corrected density functional  
852 theory. J Comput Chem. 2011;32(7):1456–65.
- 853 48. Furthmüller J, Kresse G. Efficient iterative schemes for ab initio total-energy calculations using a plane-wave  
854 basis set. Phys Rev B. 1996 Oct 15;54(16):11169–86.
- 855 49. Kresse G, Joubert D. From ultrasoft pseudopotentials to the projector augmented-wave method. Phys Rev B.  
856 1999 Jan 15;59(3):1758–75.
- 857 50. Perdew JP, Burke K, Ernzerhof M. Generalized Gradient Approximation Made Simple. Phys Rev Lett. 1996  
858 Oct 28;77(18):3865–8.

- 859 51. Thanthiriwatte KS, Hohenstein EG, Burns LA, Sherrill CD. Assessment of the Performance of DFT and DFT-  
860 D Methods for Describing Distance Dependence of Hydrogen-Bonded Interactions. *J Chem Theory Comput.*  
861 2011 Jan 11;7(1):88–96.
- 862 52. Torres E, DiLabio GA. A (Nearly) Universally Applicable Method for Modeling Noncovalent Interactions  
863 Using B3LYP. *J Phys Chem Lett.* 2012 Jul 5;3(13):1738–44.
- 864 53. Duboué-Dijon E, Mason PE, Fischer HE, Jungwirth P. Hydration and Ion Pairing in Aqueous Mg<sup>2+</sup> and Zn<sup>2+</sup>  
865 Solutions: Force-Field Description Aided by Neutron Scattering Experiments and Ab Initio Molecular  
866 Dynamics Simulations. *J Phys Chem B.* 2018 Apr 5;122(13):3296–306.
- 867 54. Kerisit S, Parker SC. Free Energy of Adsorption of Water and Metal Ions on the {1014} Calcite Surface. *J*  
868 *Am Chem Soc.* 2004 Aug 1;126(32):10152–61.
- 869 55. Galib M, Baer MD, Skinner LB, Mundy CJ, Huthwelker T, Schenter GK, et al. Revisiting the hydration  
870 structure of aqueous Na<sup>+</sup>. *J Chem Phys.* 2017 Feb 27;146(8):084504.
- 871 56. Brik MG. First-principles calculations of structural, electronic, optical and elastic properties of magnesite  
872 MgCO<sub>3</sub> and calcite CaCO<sub>3</sub>. *Phys B Condens Matter.* 2011 Feb 15;406(4):1004–12.
- 873 57. Reeder RJ, Markgraf SA. High-temperature crystal chemistry of dolomite. *Am Mineral.* 1986 Jun 1;71(5–  
874 6):795–804.
- 875 58. Ross NL, Reeder RJ. High-pressure structural study of dolomite and ankerite. *Am Mineral.* 1992 Apr 1;77(3–  
876 4):412–21.
- 877 59. Chen P-F, Chiao L-Y, Huang P, Yang Y, Liu L. Elasticity of magnesite and dolomite from a genetic algorithm  
878 for inverting Brillouin spectroscopy measurements. *Phys Earth Planet Inter.* 2006 Apr 14;155(1):73–86.
- 879 60. McGrail BP, Schaef HT, Glezakou V-A, Dang LX, Owen AT. Water reactivity in the liquid and supercritical  
880 CO<sub>2</sub> phase: Has half the story been neglected? *Energy Procedia.* 2009 Feb 1;1(1):3415–9.
- 881 61. Eliaz N, Gileadi E. *Physical Electrochemistry: Fundamentals, Techniques, and Applications.* John Wiley &  
882 Sons; 2019. 480 p.
- 883 62. King HE, Stimpfl M, Deymier P, Drake MJ, Catlow CRA, Putnis A, et al. Computer simulations of water  
884 interactions with low-coordinated forsterite surface sites: Implications for the origin of water in the inner solar  
885 system. *Earth Planet Sci Lett.* 2010 Nov 15;300(1):11–8.
- 886 63. Asaduzzaman A, Muralidharan K, Ganguly J. Incorporation of water into olivine during nebular condensation:  
887 Insights from density functional theory and thermodynamics, and implications for phyllosilicate formation  
888 and terrestrial water inventory. *Meteorit Planet Sci.* 2015;50(4):578–89.
- 889 64. de Leeuw NH, Parker SC, Catlow CRA, Price GD. Modelling the effect of water on the surface structure and  
890 stability of forsterite. *Phys Chem Miner.* 2000 May 1;27(5):332–41.
- 891 65. Pokrovsky OS, Schott J, Thomas F. Processes at the magnesium-bearing carbonates/solution interface. I. a  
892 surface speciation model for magnesite. *Geochim Cosmochim Acta.* 1999 Jul 1;63(6):863–80.
- 893 66. Kerisit S, Bylaska EJ, Felmy AR. Water and carbon dioxide adsorption at olivine surfaces. *Chem Geol.* 2013  
894 Nov 14;359:81–9.
- 895 67. Pokrovsky OS, Schott J. Processes at the magnesium-bearing carbonates/solution interface. II. kinetics and  
896 mechanism of magnesite dissolution. *Geochim Cosmochim Acta.* 1999 Jul 1;63(6):881–97.



- 897 68. Wright K, T. Cygan R, Slater B. Structure of the (101[combining macron]4) surfaces of calcite , dolomite and  
898 magnesite under wet and dry conditions. *Phys Chem Chem Phys*. 2001;3(5):839–44.
- 899 69. Michalkova A, Ilchenko M, Gorb L, Leszczynski J. Theoretical Study of the Adsorption and Decomposition  
900 of Sarin on Magnesium Oxide. *J Phys Chem B*. 2004 Apr 1;108(17):5294–303.
- 901 70. Hewlett P, Liska M. *Lea’s Chemistry of Cement and Concrete*. Butterworth-Heinemann; 2019. 898 p.
- 902 71. Jug K, Heidberg B, Bredow T. Cyclic Cluster Study on the Formation of Brucite from Periclase and Water. *J*  
903 *Phys Chem C*. 2007 Sep 1;111(35):13103–8.
- 904 72. Yeon J, van Duin ACT. ReaxFF Molecular Dynamics Simulations of Hydroxylation Kinetics for Amorphous  
905 and Nano-Silica Structure, and Its Relations with Atomic Strain Energy. *J Phys Chem C*. 2016 Jan  
906 14;120(1):305–17.
- 907 73. Water on the MgO(001) Surface: Surface Reconstruction and Ion Solvation | The Journal of Physical  
908 Chemistry Letters [Internet]. [cited 2021 May 10]. Available from:  
909 <https://pubs.acs.org/doi/abs/10.1021/acs.jpcclett.5b00885>
- 910 74. Markov IV. *Crystal Growth for Beginners: Fundamentals of Nucleation, Crystal Growth and Epitaxy*  
911 [Internet]. 2nd ed. WORLD SCIENTIFIC; 2003 [cited 2021 May 10]. Available from:  
912 <https://www.worldscientific.com/worldscibooks/10.1142/5172>
- 913 75. T. Mergelsberg S, N. Kerisit S, S. Ilton E, Qafoku O, J. Thompson C, S. Loring J. Low temperature and limited  
914 water activity reveal a pathway to magnesite via amorphous magnesium carbonate. *Chem Commun*.  
915 2020;56(81):12154–7.
- 916 76. Saldi GD, Jordan G, Schott J, Oelkers EH. Magnesite growth rates as a function of temperature and saturation  
917 state. *Geochim Cosmochim Acta*. 2009 Oct 1;73(19):5646–57.
- 918 77. Wieland E, Wehrli B, Stumm W. The coordination chemistry of weathering: III. A generalization on the  
919 dissolution rates of minerals. *Geochim Cosmochim Acta*. 1988 Aug 1;52(8):1969–81.
- 920 78. Stefánsson A, Lemke KH, Bénézech P, Schott J. Magnesium bicarbonate and carbonate interactions in aqueous  
921 solutions: An infrared spectroscopic and quantum chemical study. *Geochim Cosmochim Acta*. 2017 Feb  
922 1;198:271–84.
- 923 79. Di Tommaso D, De Leeuw NH. First Principles Simulations of the Structural and Dynamical Properties of  
924 Hydrated Metal Ions Me<sup>2+</sup> and Solvated Metal Carbonates (Me = Ca, Mg, and Sr). In: *Crystal growth &*  
925 *design* [Internet]. 2010 [cited 2021 May 10]. p. 4292–302. Available from: [http://pascal-](http://pascal-francis.inist.fr/vibad/index.php?action=getRecordDetail&idt=23347559)  
926 [francis.inist.fr/vibad/index.php?action=getRecordDetail&idt=23347559](http://pascal-francis.inist.fr/vibad/index.php?action=getRecordDetail&idt=23347559)
- 927 80. Siebert RM, Hostetler PB. The stability of the magnesium carbonate ion pair from 10 degrees to 90 degrees  
928 C. *Am J Sci*. 1977 Jun 1;277(6):716–34.
- 929 81. Hoegh-Guldberg O, Mumby PJ, Hooten AJ, Steneck RS, Greenfield P, Gomez E, et al. Coral Reefs Under  
930 Rapid Climate Change and Ocean Acidification. *Science*. 2007 Dec 14;318(5857):1737–42.
- 931 82. Lackner KS. Carbonate Chemistry for Sequestering Fossil Carbon. *Annu Rev Energy Environ*.  
932 2002;27(1):193–232.
- 933 83. Ohtaki Hitoshi, Radnai Tamas. Structure and dynamics of hydrated ions. *Chem Rev*. 1993 May 1;93(3):1157–  
934 204.

- 935 84. Obst S, Bradaczek H. Molecular Dynamics Study of the Structure and Dynamics of the Hydration Shell of  
936 Alkaline and Alkaline-Earth Metal Cations. *J Phys Chem.* 1996 Jan 1;100(39):15677–87.
- 937 85. Lam RK, England AH, Sheardy AT, Shih O, Smith JW, Rizzuto AM, et al. The hydration structure of aqueous  
938 carbonic acid from X-ray absorption spectroscopy. *Chem Phys Lett.* 2014 Oct 20;614:282–6.
- 939 86. Kumar PP, Kalinichev AG, Kirkpatrick RJ. Hydrogen-Bonding Structure and Dynamics of Aqueous  
940 Carbonate Species from Car-Parrinello Molecular Dynamics Simulations. *J Phys Chem B.* 2009 Jan  
941 22;113(3):794–802.
- 942 87. Bruneval F, Donadio D, Parrinello M. Molecular Dynamics Study of the Solvation of Calcium Carbonate in  
943 Water. *J Phys Chem B.* 2007 Oct 1;111(42):12219–27.
- 944 88. Entezari Zarandi A, Larachi F, Beaudoin G, Plante B, Sciortino M. Multivariate study of the dynamics of CO<sub>2</sub>  
945 reaction with brucite-rich ultramafic mine tailings. *Int J Greenh Gas Control.* 2016 Sep 1;52:110–9.
- 946 89. Harrison AL, Power IM, Dipple GM. Accelerated Carbonation of Brucite in Mine Tailings for Carbon  
947 Sequestration. *Environ Sci Technol.* 2013 Jan 2;47(1):126–34.
- 948 90. Zare S, Uddin KMS, Funk A, Abdolhosseini Qomi MJ. Interfacial Reaction Pathways for Docking CO<sub>2</sub> in  
949 Natural and Synthetic Rocks. *Environ Sci Technol.* 2021;Under Review.
- 950 91. Tocci G, Michaelides A. Solvent-Induced Proton Hopping at a Water–Oxide Interface. *J Phys Chem Lett.*  
951 2014 Feb 6;5(3):474–80.
- 952 92. Andrade MFC, Ko H-Y, Zhang L, Car R, Selloni A. Free energy of proton transfer at the water–TiO<sub>2</sub> interface  
953 from ab initio deep potential molecular dynamics. *Chem Sci.* 2020;11(9):2335–41.
- 954 93. Merte LR, Peng G, Bechstein R, Rieboldt F, Farberow CA, Grabow LC, et al. Water-Mediated Proton Hopping  
955 on an Iron Oxide Surface. *Science.* 2012 May 18;336(6083):889–93.
- 956 94. Wendt S, Matthiesen J, Schaub R, Vestergaard EK, Lægsgaard E, Besenbacher F, et al. Formation and  
957 Splitting of Paired Hydroxyl Groups on Reduced  $\text{TiO}_2(110)$ . *Phys Rev Lett.* 2006 Feb  
958 14;96(6):066107.
- 959 95. Comtet J, Grosjean B, Glushkov E, Avsar A, Watanabe K, Taniguchi T, et al. Direct observation of water-  
960 mediated single-proton transport between hBN surface defects. *Nat Nanotechnol.* 2020 Jul;15(7):598–604.
- 961 96. Comtet J, Rayabharam A, Glushkov E, Zhang M, Ahmet A, Watanabe K, et al. Anomalous interfacial  
962 dynamics of single proton charges in binary aqueous solutions. *ArXiv210100231 Cond-Mat [Internet].* 2021  
963 Jan 1 [cited 2021 May 17]; Available from: <http://arxiv.org/abs/2101.00231>
- 964 97. Marx D, Chandra A, Tuckerman ME. Aqueous Basic Solutions: Hydroxide Solvation, Structural Diffusion,  
965 and Comparison to the Hydrated Proton. *Chem Rev.* 2010 Apr 14;110(4):2174–216.
- 966 98. Riccardi D, König P, Prat-Resina X, Yu H, Elstner M, Frauenheim T, et al. “Proton Holes” in Long-Range  
967 Proton Transfer Reactions in Solution and Enzymes: A Theoretical Analysis. *J Am Chem Soc.* 2006 Dec  
968 1;128(50):16302–11.
- 969 99. Riccardi D, König P, Guo H, Cui Q. Proton Transfer in Carbonic Anhydrase Is Controlled by Electrostatics  
970 Rather than the Orientation of the Acceptor. *Biochemistry.* 2008 Feb 1;47(8):2369–78.
- 971 100. Zhang W, van Duin ACT. Second-Generation ReaxFF Water Force Field: Improvements in the Description  
972 of Water Density and OH-Anion Diffusion. *J Phys Chem B.* 2017 Jun 22;121(24):6021–32.

- 973 101. Tribello GA, Bonomi M, Branduardi D, Camilloni C, Bussi G. PLUMED 2: New feathers for an old bird.  
974 Comput Phys Commun. 2014 Feb 1;185(2):604–13.
- 975 102. Kumar S, Rosenberg JM, Bouzida D, Swendsen RH, Kollman PA. THE weighted histogram analysis method  
976 for free-energy calculations on biomolecules. I. The method. J Comput Chem. 1992 Oct 1;13(8):1011–21.
- 977